A 1-D morphodynamic model for rill erosion

Athanasios N. Papanicolaou,[1] John T. Sanford,[2] Dimitrios C. Dermisis,[1] and Gabriel A. Mancilla[3]

Received 4 August 2009; revised 25 March 2010; accepted 27 April 2010; published 30 September 2010.

[1] The key objective of this paper is to develop a 1-D hydrodynamic and sediment transport model, namely, RILL1D, that handles transcritical flows over abrupt changes (e.g., formation of pool crests and width change) in a single rill and also predicts changes in rill bed elevation. Replication of rill conditions in terms of flow and bed evolution changes necessitated the use of an enhanced TVD-MacCormack scheme with implementation of Tseng's surface gradient method, to provide an oscillation free solution over formed pool crests. The model at the end of each time step calculates the flow depth, velocity, and bed shear stress and provides changes in bed elevation and grain size distribution within a cell. The hydrodynamic performance of RILL1D is evaluated by comparing its results with either analytical solutions or experimental observations from various benchmark tests with rigid bed conditions that include (1) formation of a hydraulic jump in a rectangular channel, (2) steady subcritical and transcritical flow (without a shock) over a hump, (3) formation of a hydraulic jump in a converging-diverging frictionless channel, and (4) flows over step-pools. It is shown that the enhanced TVD-MacCormack scheme adequately simulates transcritical flows by preserving the mass conservation and reducing the artificial numerical error. The scheme also approximates satisfactorily depth and velocity for a single rill, with a fixed bed consisting of steps and pools, except near the pool headwalls where a backroller forms with negative velocities. The sediment component of RILL1D is evaluated by two field investigations of single rills with mobile beds. With the field data the code is tested for its ability to reproduce measured values of sediment transport rates. A sensitivity analysis is performed to assess the effects of cell size and critical erosional strength in the predictive ability of the model. RILL1D performs reasonably well in these simulations in terms of sediment prediction rates and fared adequately in terms of replicating rill bed morphology.

Citation: Papanicolaou, A. N., J. T. Sanford, D. C. Dermisis, and G. A. Mancilla (2010), A 1-D morphodynamic model for rill erosion, *Water Resour. Res.*, *46*, W09541, doi:10.1029/2009WR008486.

1. Introduction

[2] Soil erosion in a watershed is highly variable occurring at different temporal and spatial scales. Gullies and rills are considered significant contributors to erosion at the watershed scale [*De Santisteban et al.*, 2005; *Torri et al.*, 2006; *Hancock et al.*, 2007]. The focus of this study is on rill erosion, which is defined as the erosion process triggered by concentrated shallow flow within small channels, known as rills (Figure 1).

[3] From the geomorphologic point of view, rills resemble gullies and high gradient streams. However, rill erosion is greatly accelerated in time [e.g., *Foster and Meyer*, 1972; *Nearing et al.*, 1997]. As a result many of the geomorphologic features found in gullies and high gradient streams also appear in rills [e.g., *Elliot and Laflen*, 1993; *Øygarden*, 2003; *Bennett and Alonso*, 2006]. Such features include knickpoints, pools-steps (i.e., areas of locally flat, steep slopes), rough uneven bed profiles, and varying cross-sections with forming sequences of width constrictions and expansions (Figure 2). These features are dynamic due to the progression of erosion, influencing both flow and sediment transport during a runoff event.

[4] In terms of sediment transport, rills function as both sediment source areas and sediment transport conveyors. Flow in rills contributes to the erosion process in two ways: (1) it detaches sediment particles along the rill surface and (2) it transports both the sediment detached in the rills along with the lateral influx of sediment delivered to the rills due to interrill erosion. In many instances soil particles are detached from the rill surface and transported as aggregates (i.e., many fine particles held together in a single mass or cluster) [*Giménez et al.*, 2007]. The aggregates have been observed to move along the rill bed much like a bed load and are readily deposited. Single particles, being lighter than the aggregates, mainly stay in suspension [*Gilley et al.*, 1993; *Dermisis and Papanicolaou*, 2009]. The sediment yield from a rill, defined here as the volumetric rate of the eroded material that exits the rill, is dependent upon the capacity of flow to transport sediment within rills rather than

[1] IIHR-Hydroscience and Engineering, Department of Civil and Environmental Engineering, University of Iowa, Iowa City, Iowa, USA.
[2] WEST Consultants, Seattle, Washington, USA.
[3] Departamento de Silvicultura, Facultad de Ciencias, Universidad de Chile, Santiago, Chile.

0043-1397/10/2009WR008486

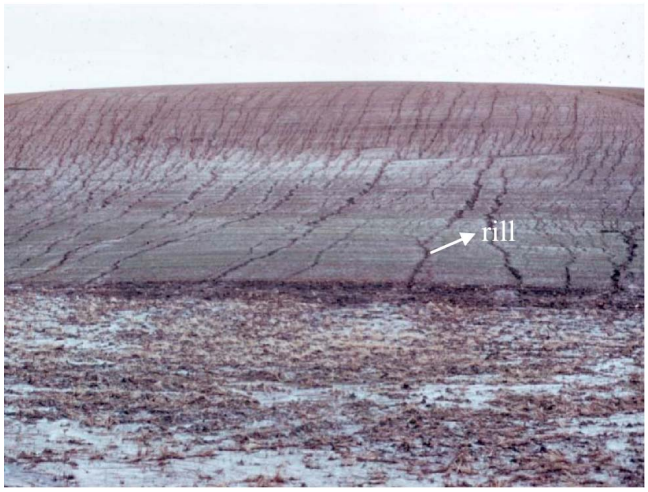

Figure 1. Deeply incised rills.

the erosion potential of the rill. Therefore, sediment yield predictions require estimates of the amount of sediment transported within rills.

[5] Because measuring transport of flow and sediment from fields and catchments requires multiple sampling locations and can be time intensive, it is desirable that dynamic predictions of flow and sediment transport are performed via numerical models [*Lei et al.*, 1998]. Previous models that simulate flow and sediment movement under shallow flow conditions were built upon simplified conservation laws, using various numerical methods to solve the governing equations [e.g., *Sanders et al.*, 2003; *Cao et al.*, 2006]. For example, *Cao et al.* [2006] have introduced a shallow water hydrodynamic model that can simulate flow, sediment transport and morphological evolution using the mass and momentum conservation equations for the water–sediment mixture along with the mass conservation equations for the bed material transport. Their model was tested successfully for mobile bed hydraulics of dam-break flows and for hyperconcentrated sediment-laden floods (i.e., "starved" floods that entrain enormous volumes of sediment from the bed triggering quick and extensive bed-tearing scour) over erodible beds. The equations that they used constituted a fourth-order hyperbolic system, solved numerically using a range of effective schemes (i.e., total variation diminishing TVD version of the second-order weighted average flux method along with an approximate Riemann solver) that can capture shocks and sharp fronts reasonably well [e.g., *Toro*, 2001; *LeVeque*, 2002]. Lately, *Bradford and Sanders* [2002] and *Sanders et al.* [2003] have used the finite volume method for discretizing the mass and momentum integral equations. Their results demonstrated an excellent ability to preserve conservation properties and to resolve discontinuous flow fields in the case of shallow water flows over arbitrary topography with moving lateral boundaries caused by flooding or recession.

[6] To predict flow and sediment movement in rills, models that replicate the physics of flow and sediment are needed. Currently, morphodynamic models treat the flow in rills as steady and uniform, while assuming both rill widths and bed slopes are time invariant and spatially uniform [e.g., *Morgan et al.*, 1998; *Flanagan and Nearing*, 2000]. However, several experimental studies show that flow in rills is spatially varied and unsteady [*Govers et al.*, 2007; *Liu et al.*, 2007]. Variable rill geometry includes flows over pool crests formed in rills and/or flows around the vicinity of protruding (or partly submerged to the flow) aggregate clods [*Tayfur*, 2002; *Giménez et al.*, 2004].

[7] Due to the limitation of accounting for the non-uniform and unsteady nature of flow in rills, existing models tend to either overestimate or underestimate the bed shear stress acting on soil particles along with the amount of sediment transported [*Tatard et al.*, 2008]. While such limitation may not have a significant impact over long-term predictions (e.g., for multiple decadal scales) of surface runoff and sediment erosion, the effects may be more pronounced for single storm predictions [*Kennedy and Schillinger*, 2006; *Abaci and Papanicolaou*, 2009].

[8] The key objective of this paper is to develop a 1-D hydrodynamic and sediment transport model to handle abrupt changes in flow (transcritical flows) found in single

Figure 2. (left) A rill formed in the IIHR-Hydroscience and Engineering laboratory. (right) The formation of rills in a hill [after *Mancilla*, 2004].

rills and predict sediment transport rates of rill beds. The structure of the flow component of RILL1D is based on the hydrodynamic model, 3ST1D, which was developed by *Papanicolaou et al.* [2004], for simulating step-pool sequences in high gradient, gravel bed streams. The key difference between RILL1D and 3ST1D is that the hydrodynamic component of RILL1D is further enhanced to allow computation of the flow depth and depth-averaged velocity without violating the flow continuity equation over abrupt changes (e.g., pool crests, aggregate clogs). As a result, the hydrodynamic improvement in RILL1D includes the modification of the total variance diminishing TVD-MacCormack scheme and implementation of the surface gradient method based on the ingenious work of *Tseng* [2003].

[9] The sediment transport component of RILL1D is completely different than that of 3ST1D, as RILL1D deals with fine sediments and includes: calculation of the critical erosional strength; calculation of the rill sediment-carrying capacity; and determination of the erosion and deposition rates. The model at the end of each time step predicts the flow depth, velocity and shear stress distribution and calculates changes in bed elevation and size distribution within a cell.

[10] The hydrodynamic component of the model is evaluated by comparing its predictions with either analytical solutions or experimental observations from various benchmark tests with rigid bed conditions. The sediment component of the model is evaluated using two field investigations of single rills with mobile beds. A sensitivity analysis is performed to assess the effects of cell size and critical erosional strength in the predictive capability of the model.

2. Methodology

2.1. Hydrodynamic Component of RILL1D

[11] RILL1D model is developed based on the following considerations.

[12] 1. Flow in rills is predominantly unidirectional [*Lei et al.*, 1998].

[13] 2. Temporal and spatial characteristics of flow can be adequately described by using the unsteady form of the 1-D Saint-Venant equations [e.g., *Tayfur et al.*, 1993]. The 1-D Saint-Venant equations express the law of conservation of mass and momentum along the flow direction [*Cunge et al.*, 1980].

[14] 3. Friction at the bed of the channel is dominant over internal flow shear stresses, and thus the latter can be considered negligible [*Brufau et al.*, 2000].

[15] 4. High gradient rills are characterized by step and pool sequences [*Foster and Meyer*, 1972]. In this case, flow becomes transcritical at the brink of the pool [*Foster and Meyer*, 1972; *Foster et al.*, 1995; *Giménez et al.*, 2004].

[16] 5. Interrill contributions are not considered herein since the focus is on concentrated flow within single rills, although it is known that the majority of flow in rills comes from interrill areas [e.g., *Tayfur and Kavvas*, 1994]. The work by *Tayfur and Kavvas* [1998] and *Tayfur* [2007] included the development of a hillslope-scale, spatially averaged model for quasi two-dimensional overland flows with interacting rill and interrill flows.

[17] 6. The effects of rain splash erosion on rill formation and flow roughness characteristics are not considered [*Lei et al.*, 1998].

[18] 7. The bed slope is considered to be time variant and spatially non-uniform. The model is capable of accounting for variable rill widths in space, however, the width of different rill segments is considered to be time invariant during the simulation period [*Lei et al.*, 1998].

[19] 8. The momentum coefficient, β, in the Saint-Venant equations can be assumed equal to 1 since flows within rills are typically shallow.

[20] 9. Surface tension can be ignored here since the soil is considered fully saturated, which is quite common for flows in rills [*Mancilla*, 2005].

[21] 10. It is applicable to cases featuring weak sediment transport and slow bed evolution.

[22] Under these assumptions the Saint-Venant equations can be written in conservative form as follows:

$$\frac{\partial \boldsymbol{U}}{\partial t} + \frac{\partial \boldsymbol{F}}{\partial x} = \boldsymbol{S} \tag{1}$$

where

$$\boldsymbol{U} = \begin{pmatrix} A \\ Q \end{pmatrix} \tag{2a}$$

$$\boldsymbol{F} = \begin{pmatrix} Q \\ \beta \dfrac{Q^2}{A} + gI_1 \end{pmatrix} \tag{2b}$$

$$\boldsymbol{S} = \begin{pmatrix} 0 \\ gI_2 + gA(S_0 - S_f) \end{pmatrix} \tag{2c}$$

where $A[x, H(x, t)]$ = wetted cross-section area of the rill; $H(x, t)$ = water depth; $Q(x, t)$ = discharge; β = momentum coefficient = 1.0; g = acceleration of gravity; I_1 = hydrostatic pressure force term that can be written

$$I_1 = \int_0^{H(x,t)} [H - \eta]\sigma(x, \eta)d\eta \tag{3}$$

with σ representing the channel width for a water depth η:

$$\sigma(x, \eta) = \frac{\partial A(x, \eta)}{\partial \eta} \tag{4}$$

[23] The term I_2 appearing in the source term (see equation (2c)) is defined as

$$I_2 = \int_0^{H(x,t)} [H - \eta]\frac{\partial \sigma(x, \eta)}{\partial x} d\eta \tag{5}$$

and S_0, S_f are the bed and friction gradients, respectively.

[24] The inclusion of the σ gradient with respect to x in equation (5) enhances our ability to simulate flows in rills with complex cross-sectional geometries such as width constrictions and expansions. The conservative form of equation (1), via equations (2c) and (5), permits momentum to be conserved along a streamline and enables the model to capture local shocks found in transcritical flows such as flows over step crests within rills [*Chaudhry*, 1993].

[25] To solve the Saint-Venant equations, the computational domain is discretized as $x_i = i\Delta x$ and $t_j = j\Delta t$, where i and j denote space (referred here as cell) and time, respectively, and Δx, Δt denote the size of the uniform mesh and time step, respectively. The TVD-MacCormack scheme is employed here to approximate the solution of the Saint-Venant equations enhanced with the surface gradient method [*Tseng*, 2003]. The TVD-MacCormack scheme utilized here is an expansion of the widely used MacCormack scheme [*MacCormack*, 1969]. The revised MacCormack scheme includes a shock-capturing method with a second order of accuracy, capable of rendering the solution oscillation free, without introducing any additional difficulty for the treatment of the source term, $\boldsymbol{S}$ [*Garcia-Navarro et al.*, 1992]. The algorithm involves a two-step procedure due to the presence of the source term, $\boldsymbol{S}$, known as the "predictor-corrector" algorithm [*Garcia-Navarro et al.*, 1992]. The dissipation term within the algorithm is then modified based on the surface gradient method proposed by *Tseng* [2003] described below.

[26] The predictor term of the Saint-Venant equations can be written as follows using the forward finite difference scheme:

$$\tilde{\boldsymbol{U}}_i = \boldsymbol{U}_i^j - \frac{\Delta t}{\Delta x}\left[\boldsymbol{F}_{i+1}^j - \boldsymbol{F}_i^j\right] + \Delta t \boldsymbol{S}_i^j \tag{6}$$

where the symbol (~) denotes the predictor step. By substituting equations (2a), (2b), (2c) in (6) we obtain the following equations for the predictor terms A_i and $\tilde{Q}_i$:

$$\tilde{A}_i = A_i^j - \frac{\Delta t}{\Delta x}\left[Q_{i+1}^j - Q_i^j\right]$$

$$\tilde{Q}_i = Q_i^j - \frac{\Delta t}{\Delta x}\left[\left(\frac{Q_{i+1}^{j^2}}{A_{i+1}^j} - \frac{Q_i^{j^2}}{A_i^j}\right) + g\left(I_{1i+1}^j - I_{1i}^j\right)\right] + g\Delta t\left[I_{2i}^j + A_i^j\left(S_{0i}^j - S_{fi}^j\right)\right]$$

[27] The corrector term of the Saint-Venant equations can be expressed using the backward scheme as follows:

$$\tilde{\tilde{\boldsymbol{U}}}_i = \boldsymbol{U}_i^j - \frac{\Delta t}{\Delta x}\left[\tilde{\boldsymbol{F}}_i^j - \tilde{\boldsymbol{F}}_{i-1}^j\right] + \Delta t \tilde{\boldsymbol{S}}_i^j \tag{7}$$

where, the symbol (≈) denotes the corrector step. By substituting equations (2a), (2b), (2c) in (7) we obtain the following equations for the corrector terms $\tilde{\tilde{A}}_i$ and $\tilde{\tilde{Q}}_i$:

$$\tilde{\tilde{A}}_i = A_i^j - \frac{\Delta t}{\Delta x}\left[\tilde{Q}_i^j - \tilde{Q}_{i-1}^j\right]$$

$$\tilde{\tilde{Q}}_i = Q_i^j - \frac{\Delta t}{\Delta x}\left[\left(\frac{\tilde{Q}_i^{j^2}}{\tilde{A}_i^j} - \frac{\tilde{Q}_{i-1}^{j^2}}{\tilde{A}_{i-1}^j}\right) + g\left(\tilde{I}_{1i}^j - \tilde{I}_{1i-1}^j\right)\right] + g\Delta t\left[\tilde{I}_{2i}^j + \tilde{A}_i^j\left(\tilde{S}_{0i}^j - \tilde{S}_{fi}^j\right)\right]$$

[28] At the end of a time step, $\boldsymbol{U}_i^{j+1}$ is calculated by averaging predicted and corrected values (equations (6) and (7)) and by adding the TVD dissipation term to provide an oscillation free solution. The dissipation term herein is modified based on the surface gradient method proposed by *Tseng* [2003], described below. Hence,

$$\boldsymbol{U}_i^{j+1} = \underbrace{\frac{1}{2}\left(\tilde{\boldsymbol{U}}_i + \tilde{\tilde{\boldsymbol{U}}}_i\right)}_{predictor-corrector\ terms} + \underbrace{\frac{1}{2}\frac{\Delta t}{\Delta x}\left(\boldsymbol{R}_{i+1/2}\boldsymbol{\Phi}_{i+1/2} - \boldsymbol{R}_{i-1/2}\boldsymbol{\Phi}_{i-1/2}\right)}_{TVD\ dissipation\ \ term} \tag{8}$$

where the matrices $\boldsymbol{R}_{i+1/2}$ and $\boldsymbol{R}_{i-1/2}$ are defined as

$$\boldsymbol{R}_{i+1/2} = \begin{bmatrix} 1 & 1 \\ \lambda_{i+1/2}^{k=1} & \lambda_{i+1/2}^{k=2} \end{bmatrix} \tag{9a}$$

$$\boldsymbol{R}_{i-1/2} = \begin{bmatrix} 1 & 1 \\ \lambda_{i-1/2}^{k=1} & \lambda_{i-1/2}^{k=2} \end{bmatrix} \tag{9b}$$

where, $\lambda_{i+1/2}^{k=1} = u_{i+1/2} + c_{i+1/2}$, $\lambda_{i+1/2}^{k=2} = u_{i+1/2} - c_{i+1/2}$, $\lambda_{i-1/2}^{k=1} = u_{i-1/2} + c_{i-1/2}$, and $\lambda_{i-1/2}^{k=2} = u_{i-1/2} - c_{i-1/2}$ and u is the depth-averaged cross-sectional velocity, determined as

$$u_{i+1/2} = \frac{\frac{Q_i}{\sqrt{A_i}} + \frac{Q_{i+1}}{\sqrt{A_{i+1}}}}{\sqrt{A_i} + \sqrt{A_{i+1}}} \tag{10a}$$

$$u_{i-1/2} = \frac{\frac{Q_i}{\sqrt{A_i}} + \frac{Q_{i-1}}{\sqrt{A_{i-1}}}}{\sqrt{A_i} + \sqrt{A_{i-1}}} \tag{10b}$$

and c is discrete approximation to the local wave celerity, calculated as

$$c_{i+1/2} = \sqrt{\frac{gA_{i+1/2}}{\sigma_{i+1/2}}} \tag{11a}$$

$$c_{i-1/2} = \sqrt{\frac{gA_{i-1/2}}{\sigma_{i-1/2}}} \tag{11b}$$

where $A_{i+1/2} = (A_i + A_{i+1})/2$, $A_{i-1/2} = (A_i + A_{i-1})/2$, $\sigma_{i+1/2} = (\sigma_i + \sigma_{i+1})/2$, $\sigma_{i-1/2} = (\sigma_i + \sigma_{i-1})/2$. The components $\boldsymbol{\Phi}_{i+1/2}$ and $\boldsymbol{\Phi}_{i-1/2}$ in equation (8) are defined as

$$\boldsymbol{\Phi}_{i+1/2} = \begin{bmatrix} \Phi_{i+1/2}^{k=1} \\ \Phi_{i+1/2}^{k=2} \end{bmatrix} \tag{12a}$$

$$\boldsymbol{\Phi}_{i-1/2} = \begin{bmatrix} \Phi_{i-1/2}^{k=1} \\ \Phi_{i-1/2}^{k=2} \end{bmatrix} \tag{12b}$$

[29] By substituting equation (2a), (9a), (9b), (12a), (12b) in (8) one can deduce the solution of A_i^{j+1} and Q_i^{j+1} at the next time level $j + 1$ equal to

$$A_i^{j+1} = \underbrace{\frac{1}{2}\left(\tilde{A}_i + \tilde{\tilde{A}}_i\right)}_{predictor-corrector\ terms} + \underbrace{\frac{1}{2}\frac{\Delta t}{\Delta x}\left[\left(\Phi_{i+1/2}^{k=1} - \Phi_{i-1/2}^{k=1}\right) + \left(\Phi_{i+1/2}^{k=2} - \Phi_{i-1/2}^{k=2}\right)\right]}_{TVD\ dissipation\ \ term} \tag{13a}$$

$$Q_i^{j+1} = \underbrace{\frac{1}{2}\left(\tilde{Q}_i + \tilde{\tilde{Q}}_i\right)}_{predictor-corrector\ terms} + \underbrace{\frac{1}{2}\frac{\Delta t}{\Delta x}\left[\left(\lambda_{i+1/2}^{k=1}\Phi_{i+1/2}^{k=1} - \lambda_{i-1/2}^{k=1}\Phi_{i-1/2}^{k=1}\right) + \left(\lambda_{i+1/2}^{k=2}\Phi_{i+1/2}^{k=2} - \lambda_{i-1/2}^{k=2}\Phi_{i-1/2}^{k=2}\right)\right]}_{TVD\ dissipation\ \ term} \quad (13b)$$

[30] For brevity purposes, only the calculation of the term $\Phi_{i+1/2}^{k=1,2}$ is presented. Similarly, one can calculate the term $\Phi_{i-1/2}^{k=1,2}$. The component $\Phi_{i+1/2}^{k}$ for $k = 1, 2$ is given from the following equation:

$$\Phi_{i+1/2}^{k} = \psi\left(\lambda_{i+1/2}^{k}\right)\left(1 - \frac{\Delta t}{\Delta x}\left|\lambda_{i+1/2}^{k}\right|\right)\left[1 - \varphi\left(r_{i+1/2}^{k}\right)\right]\alpha_{i+1/2}^{k} \quad (14)$$

where the function ψ in equation (14) is an entropy correction to $\lambda_{i+1/2}^{k}$, and in its simplest expression takes the form

$$\psi(\lambda_{i+1/2}^{k}) = \left|\lambda_{i+1/2}^{k}\right| \qquad if\ \left|\lambda_{i+1/2}^{k}\right| \geq \varepsilon \quad (15a)$$

$$\psi(\lambda_{i+1/2}^{k}) = \varepsilon \qquad if\ \left|\lambda_{i+1/2}^{k}\right| < \varepsilon \quad (15b)$$

where ε is a small positive number whose value must be determined for each individual problem. *Harten and Hyman* [1983] suggested a formula to calculate ε, which eliminates trial and error attempts:

$$\varepsilon_{i+1/2}^{k} = \max\left|0, \lambda_{i+1/2}^{k} - \lambda_{i}^{k}, \lambda_{i+1}^{k} - \lambda_{i+1/2}^{k}\right| \quad (15c)$$

[31] The function ψ prevents the appearance of non-pragmatic hydraulic jumps (i.e., those in which energy increases across the shock), which are admissible for a classical MacCormack scheme [*Yee*, 1989].

[32] Finally, the factor φ in equation (14) is a limiter parameter responsible for obtaining non-oscillatory solutions despite the presence of strong gradients or shocks:

$$\varphi\left(r_{oi+1/2}^{k}\right) = \begin{Bmatrix} \min\left(\left|r_{oi+1/2}^{k}\right|, 1\right), & r_{oi+1/2}^{k} > 0 \\ 0, & r_{oi+1/2}^{k} \leq 0 \end{Bmatrix} \quad (16a)$$

[33] It is a nonlinear function of the ratio

$$r_{oi+1/2}^{k} = \frac{\alpha_{i+1/2-s}^{k}}{\alpha_{i+1/2}^{k}} \qquad s = \mathrm{sign}(\lambda_{i+1/2}^{k}) \quad (16b)$$

where $\alpha_{i+1/2}^{k}$ is a characteristic variable that has been incorporated in the TVD dissipation term in order to eliminate or reduce the artificial numerical error introduced by applying the TVD corrections to equations (8), (13a), and (13b). According to *Tseng* [2003], it is more suitable to express $\alpha_{i+1/2}^{k}$ as a function of the water surface elevation, $WSE = H + z$ (where z = bed elevation), instead of depth, H, for simulating open channel flows over abrupt geometries, such as the ones encountered in rills. Based on the improved surface gradient method,

$$\alpha_{i+1/2} = \begin{bmatrix} \alpha_{i+1/2}^{k=1} \\ \alpha_{i+1/2}^{k=2} \end{bmatrix} = \frac{1}{2c_{i+1/2}}\begin{bmatrix} -\lambda_{i+1/2}^{k=2} & 1 \\ \lambda_{i+1/2}^{k=1} & -1 \end{bmatrix}\begin{bmatrix} WSE_{i+1} - WSE_i \\ (Hu)_{i+1} - (Hu)_i \end{bmatrix} \quad (17)$$

[34] The described scheme must satisfy the Courant-Friedrich-Lewy (CFL) criterion at each cell in order to be stable. The CFL criterion is defined as

$$C_{ni}^{j} = \frac{\Delta \mathrm{t}}{\Delta \mathrm{x}}\left(\left|u_i^{j}\right| + c_i^{j}\right) \leq 1 \quad (18)$$

where C_{ni}^{j} is the Courant number at cell i and at time step j. In general, the value of C_n must be less than or equal to 1. If the source term, $\boldsymbol{S}$, in equation (1) obtains significant values, it is recommended that the C_n value be adjusted to values smaller than 1 in order to maintain model stability [*Brufau et al.*, 2000].

[35] The source terms S_0 and S_f appearing in the right hand side of equation (1) at each step are evaluated with forward and backward differences as follows:

Predictor step

$$S_{0i}^{j} = \frac{z_i^{j} - z_{i+1}^{j}}{\Delta x}, \quad S_{fi}^{j} = \frac{n_i^2 Q_{i+1/2}^{j}\left|Q_{i+1/2}^{j}\right|}{A_{i+1/2}^{j^2} R_{i+1/2}^{j^{4/3}}} \quad (19a)$$

Corrector step

$$S_{0i}^{j} = \frac{z_{i-1}^{j} - z_i^{j}}{\Delta x}, \quad S_{fi}^{j} = \frac{n_i^2 Q_{i-1/2}^{j}\left|Q_{i-1/2}^{j}\right|}{A_{i-1/2}^{j^2} R_{i-1/2}^{j^{4/3}}} \quad (19b)$$

where z is the bed elevation, the coefficient n denotes the Manning's resistance coefficient and R denotes the hydraulic radius.

[36] Within a cell i at time j the bed shear stress, τ_o, is calculated as

$$\tau_{oi}^{j} = \frac{f_i^{j}}{8}\rho \mathrm{u}_i^{j^2} \quad (20)$$

where f is the Darcy-Weisbach coefficient, and ρ is the density of water. The Darcy-Weisbach friction factor, f, is calculated via Manning's n, using the following equality [*Thorne and Zevenbergen*, 1985]:

$$\left(8/f_i^{j}\right)^{1/2} = \left(R_i^{j}\right)^{1/6}/n_i g^{1/2} \quad (21)$$

2.2. Sediment Component of RILL1D

[37] Sediment routing within a cell i, includes the following steps: (1) determination of the critical erosional strength of the soil, (2) determination of the carrying capacity and rill detachment in terms of units of volume, (3) determination of the erosion and depositional depths in terms of units of volume, and (4) updating the active layer thickness (defined as the bed layer where sediment is exchanged between the bed and the flow) and the bed size fraction after deposition or scour has occurred.

2.2.1. Critical Erosional Strength

[38] The critical erosional strength, τ_c, is defined as the strength provided by interparticle forces of attraction or repulsion acting at the microscopic level, including electrostatic forces, van der Waals forces, hydration forces and biological forces [*Black et al.*, 2002; *Partheniades*, 2009]. A complete identification of the properties (e.g., pH of the pore fluid; soil organic matter; clay mineralogy; soil water content) that are believed to affect the critical erosional strength of soils is provided in a number of publications [e.g., *Gilley et al.*, 1993; *Papanicolaou et al.*, 2007; *Thoman and Niezgoda*, 2008] but is not the focus of this paper.

[39] In this study, the critical erosional strength of soils, τ_c, is incorporated in the sediment algorithm with the inclusion of the widely accepted relations of *Alberts et al.* [1995]. For bare cropland surface soils containing 30% or more sand, the critical erosional strength, τ_c (Pa), is

$$\tau_c = 2.67 + 6.5\,clay - 5.8\,vfs \tag{22a}$$

where *clay* and *vfs* are the fractions of clay and very fine sand respectively. Whereas for cropland soils containing less than 30% sand:

$$\tau_c = const. \tag{22b}$$

[40] In this case, we either consider the proposed by *Alberts et al.* [1995] *const.* = 3.5 Pa or we use site specific values reported in the literature (as is the case for the *Mancilla* [2004] experiments described later).

2.2.2. Sediment-Carrying Capacity

[41] Determination of the sediment-carrying capacity remains a challenge for modeling sediment transport in shallow flows (i.e., flows in rills) [e.g., *Nord and Esteves*, 2007], because the majority of capacity equations have been developed for river flows [e.g., *Mancilla*, 2004].

[42] An extensive comparison of the available transport capacity equations by *Alonso et al.* [1981], *Foster et al.* [1995], *Cochrane and Flanagan* [1997], and *Mancilla* [2004] concluded that the *Yalin* [1977] equation provided the most acceptable results for shallow flow conditions found in rills under transport- and supply limited conditions. The *Yalin* [1977] model can be expressed as

$$\frac{T_c}{(SG)d_{50}\rho^{0.5}\tau_o^{0.5}} = 0.635 \cdot \left[1 - \frac{1}{\beta_o}\ln(1+\beta_o)\right]$$

where

$$\beta_o = 2.45^*(SG)^{-0.4}(\tau_c^*)^{0.5}\delta \tag{23a}$$

$$\delta = \frac{\tau^*}{\tau_c^*} - 1 \tag{23b}$$

$$\tau^* = \frac{\tau_o/\rho}{(SG-1)gd_{50}} \tag{23c}$$

$$\tau_c^* = \frac{\tau_c/\rho}{(SG-1)gd_{50}} \tag{23d}$$

where T_c (kg/s/m) is the determined sediment transport capacity; SG the particle specific gravity; d_{50} (m) is the median diameter of the particle; τ_o(Pa) is the bed shear stress exerted by the fluid on the sediment particles determined via equation (20); τ^* denotes the dimensionless bed shear stress acting on the rill bed; τ_c^* is the dimensionless critical shear stress (or dimensionless critical fluvial erosional strength); τ_c (Pa) is the dimensional critical erosional strength determined via equation (22a) or equation (22b) depending on the percentage of sand; and β_o and δ are dimensionless parameters reflecting soil properties [*Foster and Meyer*, 1972; *Alonso et al.*, 1981; *Finkner et al.*, 1989].

2.2.3. Sediment Erosion and Deposition

[43] RILL1D uses a steady state sediment continuity equation to describe the movement of sediment in a rill:

$$\frac{dG(x)}{dx} = D_f + D_i \tag{24}$$

where x (m) represents distance downslope, G (kg/s/m) is the transported sediment load, and D_f (kg/s/m^2) denotes the rill erosion rate per unit area. Based on the previously discussed model considerations in section 2.1, the interrill contributions, D_i, are not considered herein and D_i is set equal to zero.

[44] Considering the equations developed by *Foster et al.* [1995] for the Water Erosion Prediction Project (WEPP) model, the rate of rill erosion, D_f, can be positive for detachment and negative for deposition. Net soil detachment in rills is calculated for the case when hydraulic shear stress, τ_o, exceeds the critical erosional strength, τ_c, of the soil and the same time the sediment load, G, is less than the sediment transport capacity, T_c. Net deposition in a rill is computed when the sediment load, G, is greater than T_c. Thus, the rill erosion rate, D_f (kg/s/m^2), is calculated using the following set of equations [*Foster et al.*, 1995]:

$$\begin{cases} D_f = K_r(\tau_o - \tau_c)\left(1 - \dfrac{G}{T_c}\right) & \text{when } \tau_o > \tau_c \text{ and } G < T_c \\ D_f = \dfrac{\chi V_f}{q}(T_c - G) & \text{when } G > T_c \end{cases} \tag{25}$$

where K_r (s/m) is a rill erodibility parameter that is dependent on the soil properties, V_f (m/s) is the effective fall velocity for the sediment, q (m^2/s) is the unit discharge in the rills, and χ (~0.5) is a raindrop-induced turbulent coefficient [*Lindley et al.*, 1995].

2.2.4. Treatment of the Bed Layer

[45] In RILL1D the cells consist of three distinct regions: the flow region, where sediment is routed downstream with the flow; the active layer, where sediment is exchanged between the bed and the flow; and the parent layer, which is considered to be infinitely deep and supplies sediment to the active layer. Figure 3 shows the domain of the model and the description of a representative cell. The treatment of the bed layer, within a cell i, includes the following steps: (1) quantification of the available material within the active layer, (2) determination of the incoming sediment along with the sediment that can be carried by the flow, (3) calculation of scour and depositional depths, and (4) update of the active bed layer thickness after deposition or scour occurs. Within the cell i different sediment class sizes (p) and densities (r) will deposit or erode depending on the existing flow conditions, sediment incipient conditions, and bed roughness.

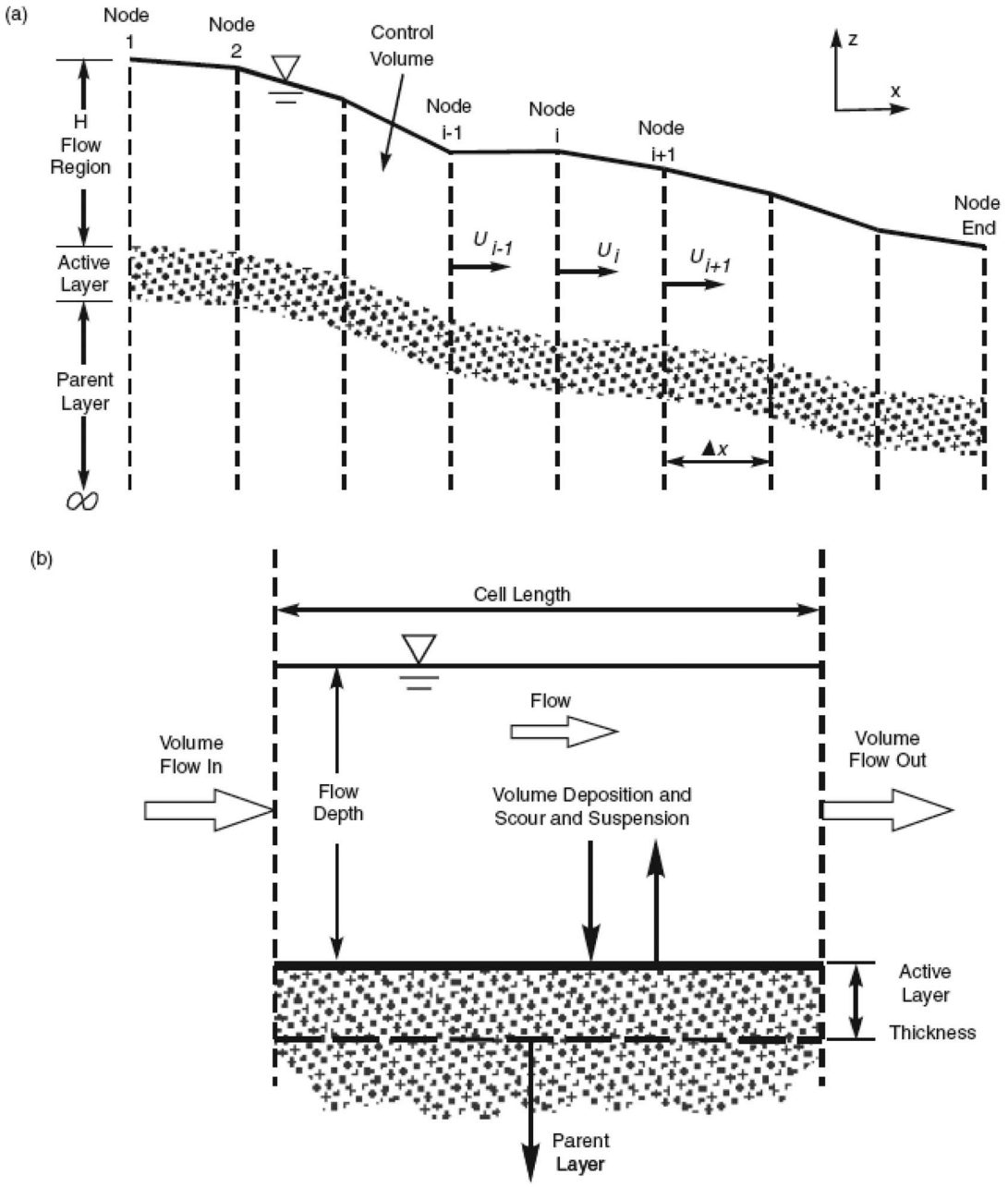

Figure 3. Schematic of (a) the computational mesh used in RILL1D and (b) the active layer concept.

[46] The volume of the available material within the active (*ACT*) layer of the cell *i*, $(\forall_{ACTpr})_i^j$, is estimated as

$$\left(\forall_{ACT_{pr}}\right)_i^j = \left(D_A F_{pr}(1-\theta)A_{bed}\right)_i^j \tag{26}$$

where D_A is the active layer thickness, F_{pr} is the percentage of the available particles with size class *p* and density *r*, θ is the porosity of the soil, and A_{bed} is the rill bed area. To determine if scour or deposition will occur for a given sediment class *p*, *r* within the cell *i* at time *j*, first the sediment-carrying capacity (defined in equation (23)) is calculated in terms of units of volume as

$$\left(\forall_{sb_{pr}}\right)_i^j = \left(T_c b \Delta t/(\rho_s)_r\right)_i^j \tag{27}$$

where *b* is the cell width of the sediment bed (*sb*) and ρ_s is the sediment particle density. The volume of sediment-carrying capacity is compared to the volume of the inflow (*IN*) sediment particles $(\forall_{IN_{pr}})_i^j$ of the same class.

[47] If the volume of transport capacity $(\forall_{sb_{pr}})_i^j$ exceeds the volume inflow for the given class $(\forall_{IN_{pr}})_i^j$, then that class size will scour from the bed. To calculate the amount of scour, the volume of excess capacity (*EC*) is determined as

$$\left(\forall_{EC_{pr}}\right)_i^j = \left(\forall_{sb_{pr}}\right)_i^j - \left(\forall_{IN_{pr}}\right)_i^j \tag{28}$$

and compared to the rill detachment (*DR*) volume calculated as

$$\left(\forall_{DR_{pr}}\right)_i^j = \left(D_f \Delta t \Delta x b/(\rho_s)_r\right)_i^j \tag{29}$$

where D_f is calculated from equation (25). The lesser of these two values will limit the amount of scour. The scour (SC) volume $(\forall_{SC_{pr}})_i^j$ within the cell i for the sediment p, r is determined as follows:

$$\left(\forall_{SC_{pr}}\right)_i^j = \begin{cases} \left(\forall_{EC_{pr}}\right)_i^j & if \quad \left(\forall_{EC_{pr}}\right)_i^j \le \left(\forall_{DR_{pr}}\right)_i^j \\ \left(\forall_{DR_{pr}}\right)_i^j & if \quad \left(\forall_{EC_{pr}}\right)_i^j > \left(\forall_{DR_{pr}}\right)_i^j \end{cases} \tag{30}$$

[48] This method prohibits the scour volume from exceeding the sediment-carrying capacity of the flow. The scour depth is determined as

$$\left(SC_{pr}\right)_i^j = \left(\forall_{SC_{pr}}/b\Delta x\right)_i^j \tag{31}$$

and the volume of sediment with class p, r that exits the cell is

$$\left(\forall_{OUT_{pr}}\right)_i^j = \left(\forall_{SC_{pr}}\right)_i^j + \left(\forall_{IN_{pr}}\right)_i^j \tag{32}$$

[49] If the calculated transport capacity is less than the volume inflow for the sediment class p, r then deposition occurs, and the volume of deposition rate is

$$\left(\forall_{DR_{pr}}\right)_i^j = \left(D_f \Delta t \Delta x b/(\rho_s)_r\right)_i^j \tag{33}$$

where, D_f is calculated from equation (25). The volume of deposition (DP) is

$$\left(\forall_{DP_{pr}}\right)_i^j = \left(\forall_{DR_{pr}}\right)_i^j \tag{34}$$

and the volume of sediment with class p, r that exits (OUT) the cell is

$$\left(\forall_{OUT_{pr}}\right)_i^j = \left(\forall_{IN_{pr}}\right)_i^j - \left(\forall_{DP_{pr}}\right)_i^j \tag{35}$$

[50] The deposition depth is expressed here as

$$\left(DP_{pr}\right)_i^j = \left(\forall_{DP_{pr}}/b\Delta x\right)_i^j \tag{36}$$

[51] For all cases, it is verified that the sediment continuity is satisfied within the cell i for the sediment class p, r at time j, viz.,

$$\left(\forall_{OUT_{pr}}\right)_i^j - \left(\forall_{IN_{pr}}\right)_i^j - \left(\forall_{DP_{pr}}\right)_i^j + \left(\forall_{SC_{pr}}\right)_i^j = 0 \tag{37}$$

[52] In order to update the active bed layer thickness after deposition or scour occurs, the total deposition or scour depth is compared with that of the active layer. If the total deposited layer $\sum_{p=1,r=1}^{N,M} (DP_{pr})_i^j = (\forall_{DR_{pr}})_i^j$, where N denotes the maximum number of sediment size classes and M is the maximum number of sediment size densities, is thicker than the active thickness $(D_A)_i^j$, then the active layer thickness at $j + 1$ is equal to

$$(D_A)_i^{j+1} = \sum_{p=1,r=1}^{N,M} (DP_{pr})_i^j \tag{38}$$

[53] If only scour takes place, then the updated active layer thickness is given as

$$(D_A)_i^{j+1} = (D_A)_i^j - \sum_{p=1,r=1}^{N,M} (SC_{pr})_i^j \tag{39}$$

[54] In the event that parts of the total fraction of sediments deposit and other parts scour, the total scour depth and total deposition depth are summed and compared to determine if net deposition or scour occurred within the cell i. The change in bed elevation within cell i at time j is determined as follows:

$$\Delta EL_i^j = \frac{\sum_{p=1,r=1}^{N_1,M} \left(DP_{pr}\right)_i^j - \sum_{p=1,r=1}^{N_2,M} \left(SC_{pr}\right)_i^j}{\theta} \tag{40}$$

where $N_1 + N_2 = N$, and the updated active layer thickness is given as

$$(D_A)_i^{j+1} = \begin{cases} (D_A)_i^j + \sum_{p=1,r=1}^{N_1,M} (DP_{pr})_i^j - \sum_{p=1,r=1}^{N_2,M} (SC_{pr})_i^j \\ \quad - F_{pr}^j \left(D_{Ai}^j - \Delta EL_i^j\right)\theta, \quad \Delta EL_i^j \ge 0 \\ (D_A)_i^j + \sum_{p=1,r=1}^{N_1,M} (DP_{pr})_i^j - \sum_{p=1,r=1}^{N_2,M} (SC_{pr})_i^j \\ \quad + F_{pr}^j \left|\Delta EL_i^j\right|\theta, \quad \Delta EL_i^j < 0 \end{cases} \tag{41}$$

2.3. Execution of the Model

[55] In this section, first, a brief description of the components of the computer code is provided; the executable program is written in an emacs20 editor, and compiled with a Compaq Visual Fortran compiler for Microsoft Windows XP. The initial and boundary conditions are entered into the program by means of two text files; the bed_initial.dat and the xsect.dat. The bed_initial.dat file contains rill bed information including particle size, specific gravity, value for Manning's n and percent of each size and specific gravity in the parent and initial active layers (Figure 3). The xsect.dat file contains the cross-sectional information such as bed width, top width, elevation, and channel side slope if the channel geometry changes with the longitudinal direction. The computer program is capable of handling up to five different specific gravities and 20 sediment size classes. The initial conditions and boundary conditions are contained in the file bc.dat. This file contains information about the total reach length of the rill that is modeled, the rill cross-sectional geometry if constant (side slopes, bed slope, bed width), temperature, flow discharge at the upstream end, depth at the downstream end, bed porosity, and number of cells. The flowchart in Figure 4 depicts the different components of RILL1D, the preprocessor unit where the initial and boundary conditions are provided, the main processor unit where the hydrodynamic, sediment, and update of bed changes in the active layer are processed, and the post processor unit where the output of the results is obtained.

3. Results

[56] In order to examine the validity of RILL1D, first the hydrodynamic component of the model was checked in

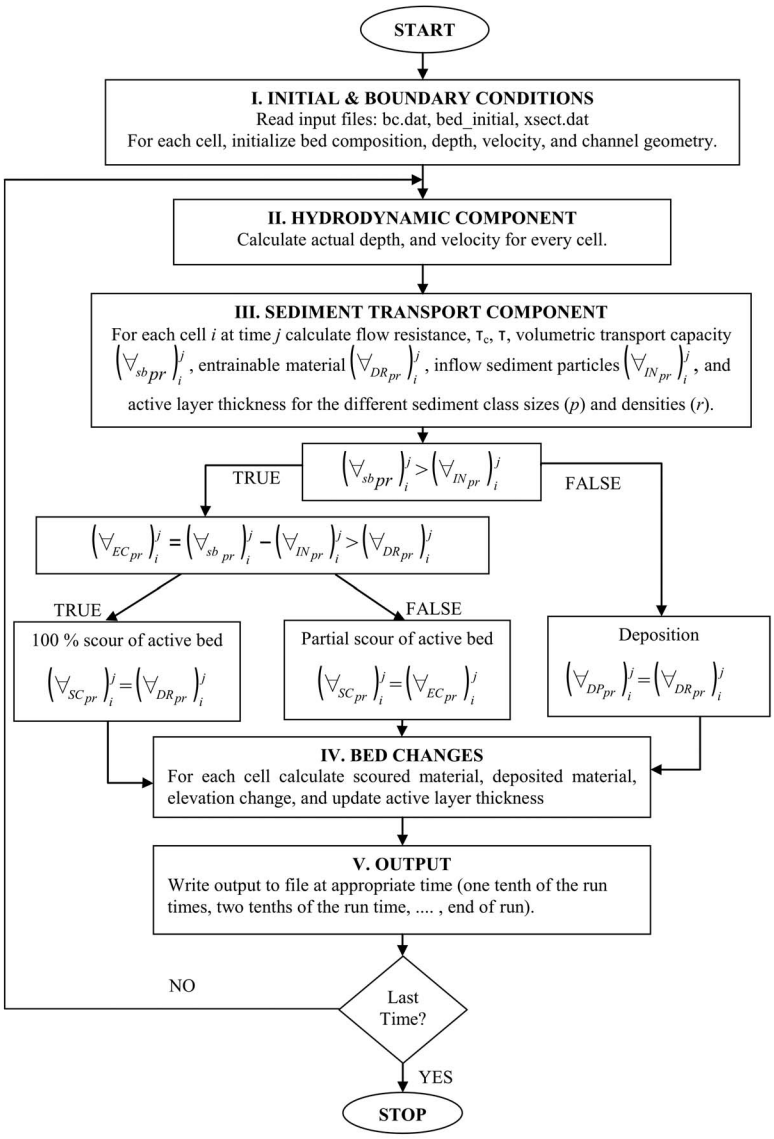

Figure 4. Flowchart of the RILL1D model.

cases of rigid bed conditions. Next, the sediment component of RILL1D was tested for modeling flows and sediment transport in erodible rills.

3.1. Numerical Tests to Examine the Hydrodynamic Component of RILL1D

[57] To examine the capability of the enhanced TVD-MacCormack scheme in predicting the water surface profile for rigid bed conditions, the following benchmark tests for steady flow conditions were performed. Test 1 relates to the formation of a hydraulic jump in a rectangular channel. Tests 2a and 2b represent the case of a steady subcritical and transcritical flow (without a shock) over a hump, respectively. Test 3 illustrates the case of a hydraulic jump formation in a converging-diverging frictionless channel. Tests 4a and 4b examined flows over step-pool sequences. Tests 2–4 were also used to test the model's capability to preserve mass along the channel [e.g., *Vázquez-Cendón*, 1999; *Tseng*, 2003; *Catella et al.*, 2008]. The accuracy of the presented scheme is demonstrated by comparing the numerical solutions with either analytical solutions or experimental observations. Table 1 provides a summary of the hydraulic conditions used in tests 1–4.

3.1.1. Test 1: Hydraulic Jump in a Rectangular Channel

[58] The numerical scheme is applied here to simulate five different experimental runs conducted by *Gharangik and Chaudhry* [1991]. Their experiments were performed in a wide, rectangular, horizontal, re-circulating flume, having a length of 14 m, width of 0.46 m and height of 0.915 m. *Gharangik and Chaudhry* [1991] observed the formation and location of a hydraulic jump for Froude numbers ranging from 2.3 to 7.0 and downstream flow depths ranging from 0.168 m to 0.286 m. For the range of Froude numbers tested, the values of Manning's *n* coefficients used in the simulations were between 0.006 and 0.008, since the bottom flume was made of metal and the sidewalls

Table 1. Summary of the Benchmark Tests for Rigid Bed Conditions

Test	Run Number	Longitudinal Distance (m)	Width (m)	Slope (m/m)	Depth, $H_{upstream}$ (m)	Depth, $H_{downstream}$ (m)	Discharge (m^3/s)	Manning's Roughness
Test 1: Hydraulic jump in a rectangular channel [*Gharangik and Chaudhry*, 1991]	1	14	0.460	0	0.031	0.265	0.05460	0.008
	2	14	0.460	0	0.024	0.195	0.03594	0.007
	3	14	0.460	0	0.040	0.286	0.06584	0.0075
	4	14	0.460	0	0.043	0.222	0.05414	0.008
	5	14	0.460	0	0.064	0.168	0.05376	0.006
Test 2a: Steady subcritical flow over a hump atop a frictionless bed [e.g., *Vázquez-Cendón*, 1999]	1	25	1.00	Varied (hump)	-	2.00	4.42	no friction
Test 2b: Steady transcritical flow over a hump atop a frictionless bed [e.g., *Tseng*, 2003]	1	1,000	-	Varied (hump)	-	1.56	20 (unit discharge)	no friction
Test 3: Steady transcritical flow on a converging-diverging channel [e.g., *Vázquez-Cendón*, 1999]	1	500	Varied	0	2.00	1.87	20	no friction
Test 4a: Shallow water transcritical flows [*Tseng*, 2003]	1	1,600	-	Varied (step-pool)	-	0.420	0.590 (unit discharge)	0.033
Test 4b: Shallow water transcritical flows [*Giménez et al.*, 2004]	1	1.8	Varied	Varied (step-pool)	0.023	0.078	0.001	0.030–0.040

were constructed of glass [*Gharangik and Chaudhry*, 1991]. The number of cells among the different tests ranged between 50 and 100. The flow depth and discharge at the upstream side and the flow depth at the downstream side were imposed as boundary conditions in the model (Table 1). Figures 5a–5e show the jump locations to be captured for all runs within ±20 cm from the measured jump crest (the standard deviation from the measured vertical front was ~13 cm). The computed steady water surface profiles reasonably agree with the experimental measurements (average error of ~1.5%).

3.1.2. Test 2a: Steady Subcritical Flow Over a Frictionless Bed Hump

[59] This test demonstrates a steady frictionless flow with a bell-shaped hump at the channel bottom, representing irregular bottom topography [e.g., *Vázquez-Cendón*, 1999]. An analytical solution can be derived from the conservation of mass and energy. The channel is 25 m long and 1 m wide with rectangular cross sections and frictionless bottom topography, $z(x)$,defined by the following equation:

$$z(x) = \begin{cases} 0\,\text{m}, & x < 8\,\text{m} \text{ and } x > 12\,\text{m} \\ 0.2 - 0.05 \cdot (x-10)^2\,\text{m}, & 8\,\text{m} \le x \le 12\,\text{m} \end{cases} \tag{42}$$

[60] The bell-shaped hump starts at x = 8 m and ends at x = 12 m, as shown in Figure 6a. The numerical simulation of this test was performed using 100 cells. At the upstream end, a discharge of Q = 4.42 m^3/s was imposed and the downstream depth was set equal to 2.00 m. Figure 6a compares the simulation results of water surface elevation with the analytical solution. As it can be seen, there is a perfect agreement (error = 0%) between the analytical solution and the numerical solution. Figure 6b shows a variation of discharge along the channel, implying that mass conservation is preserved even for the channel flows comprised of irregular bottom topography.

3.1.3. Test 2b: Steady Transcritical Flow Over a Frictionless Bed Hump Without a Shock

[61] Similarly to Test 2a, herein we present the case of transcritical flows over a bell-shaped hump (without a shock) at the channel bottom [e.g., *Tseng*, 2003]. An analytical solution can be derived from the conservation of mass and energy. The channel length is 1,000 m and the bell-shaped hump exists between x = 125 m and x = 875 m. The bed elevation, $z(x)$, of the channel shown in Figure 7a can be described as

$$z(x) = 4.75 \sin^2\left(\frac{x-125}{750}\pi\right) \tag{43}$$

[62] The numerical simulation of this test was performed using 100 cells. At the upstream end, a unit discharge of q = 20 m^2/s was imposed and the downstream depth was set equal to 1.56 m. Figure 7a shows that there is a perfect agreement (error < 0.01%) between the analytical and numerical solutions. Figure 7b shows that mass conservation is preserved even for transcritical flow conditions.

3.1.4. Test 3: Steady Flow in a Converging-Diverging Frictionless Channel

[63] The numerical test is performed to investigate the efficiency of the numerical scheme involving variations on the channel width. The width variation modifies the steady state profiles and due to the boundary conditions a stationary hydraulic jump appears to connect subcritical and supercritical flows [e.g., *Vázquez-Cendón*, 1999]. The length of the horizontal channel is 500 m and the width variation, $B(x)$, is characterized by the following sinusoidal function:

$$B(x) = \begin{cases} 5 - 0.7065\left(1 + \cos\left(2\pi\left(\dfrac{-250}{300}\right)\right)\right), & |x-250| \le 150 \\ 5, & \text{otherwise} \end{cases} \tag{44}$$

[64] At the upstream end, a discharge of Q = 20 m^3/s and a depth of 2.0 m was imposed and the downstream depth was set equal to 1.87 m. In this test the numerical simulation was performed using 200 cells. Figure 8a compares the simulation results of water surface elevation with the analytical solution. Based on these results, there is an excellent agreement between the analytical solution and the numerical solution and RILL1D handles the formation of a stationary shock without any numerical oscillations. The relative errors between the exact and numerical solutions in the water

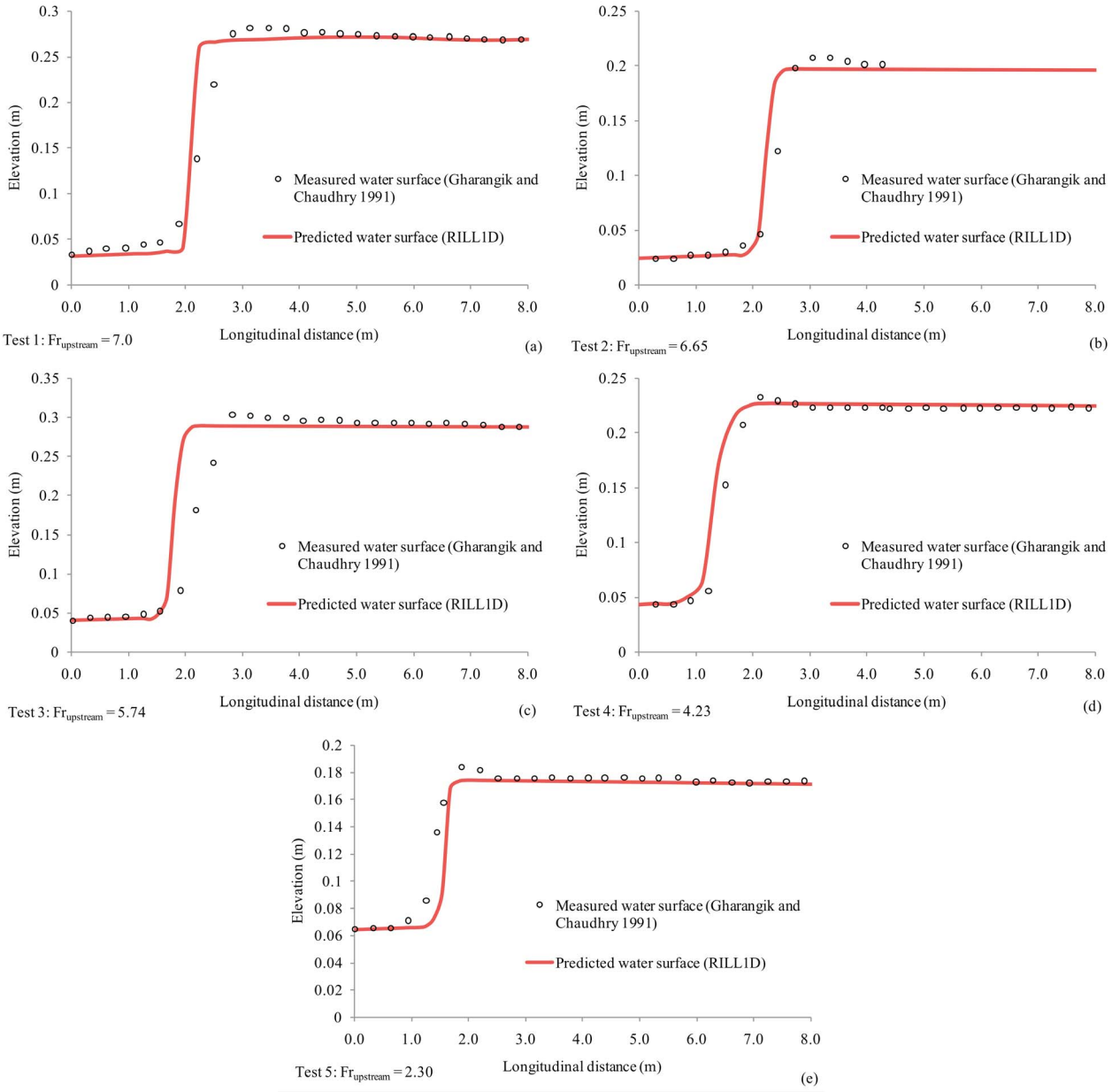

Figure 5. (a–e) Water surface profiles of the formation of hydraulic jumps for 5 different Froude numbers in a rectangular, horizontal channel (only the first 8 m of the channel are shown). Solid lines show the results from the RILL1D simulations and points show the experimental data by *Gharangik and Chaudhry* [1991].

surface elevation and discharge are plotted in Figures 8b and 8c. The maximum relative errors in terms of the water surface elevation and discharge are <3.0% and 1.0%, respectively.

3.1.5. Test 4: Flows Over Step-Pools

[65] Numerical simulations were performed using the following data sets: *Tseng*'s [2003] case of transcritical flow in irregular bed topography of a natural channel and *Giménez et al.*'s [2004] case of transcritical flow over a fixed rill bed with step-pool sequences formed in the laboratory. Both experiments deal with varying flows over step-pool sequences. However, in the *Giménez et al.* [2004] case, the flow depth is shallow (on an average 2.0 cm).

3.1.5.1. Experimental Data Set 1: Simulation of the *Tseng* [2003] Case

[66] The configuration used by *Tseng* [2003] is commonly found in natural mountain rivers with a step-pool sequence. The length of the channel is 1,600 m long, the Manning's coefficient is 0.033, and the bottom topography of the channel is shown in Figure 9a. At the upstream end, a constant unit discharge of q = 0.59 m^2/s is imposed, while the downstream water depth is set at the value of 0.42 m. A uniform grid size of Δx = 8 m (200 cells) was used in the simulation. Figure 9a displays the variation of simulated water surface elevations along the channel. It shows that RILL1D can adequately simulate the transcritical flow by

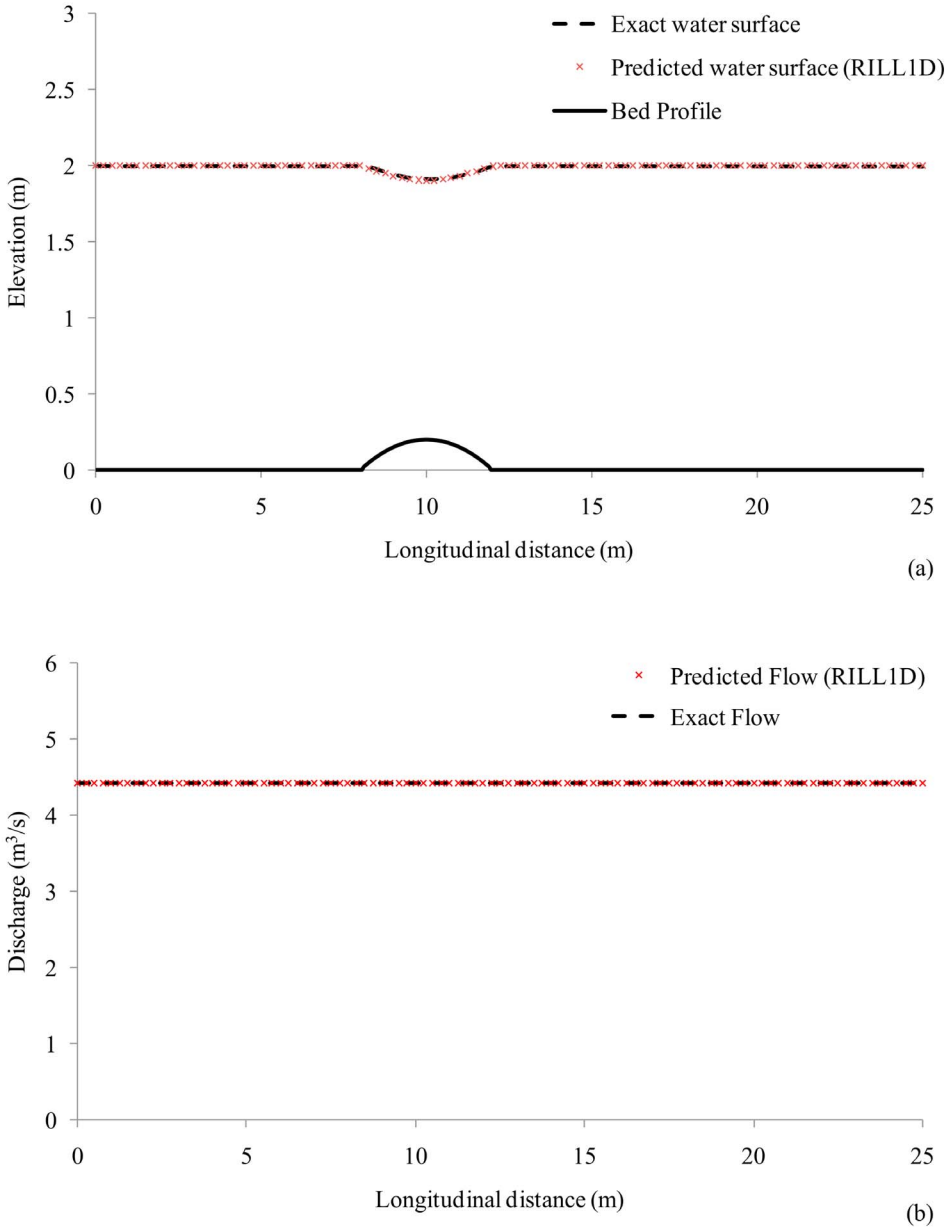

Figure 6. (a) Water surface profile of subcritical flow in a rectangular, horizontal channel over a hump. Solid line shows the results from the RILL1D simulations and the dashed line provides the exact solution. (b) Flow continuity was preserved along the channel length.

reducing the artificial numerical error due to the irregular topography and the shallow flow depth conditions. Also, as shown in Figure 9b, the continuity equation is satisfied along the whole reach. The average relative error in terms of discharge is less than 0.3%.

3.1.5.2. Experimental Data Set 2: Simulation of the *Giménez et al.* [2004] Flume Study

[67] This experiment was conducted under controlled conditions in a laboratory flume by *Giménez et al.* [2004]. The goal was to compare the predicted and experimentally determined flow depth and time-averaged velocity over a fixed rill bed. The *Giménez et al.* [2004] experiments provide bed bathymetry measurements, point time-averaged streamwise velocities, and flow depth along the longitudinal direction of the rill.

[68] The experiment was carried out in a tilting laboratory flume 4.5 m long, 0.45 m wide, and 0.45 m deep with a useful test section of 2.5 m. The lower point two meters of the flume was filled with a silt loam soil, which was compacted to form a sub soil. The upper 0.25 m part of the test section was filled with the same soil but sieved at 20 mm in order to develop fine seedbed conditions.

[69] A rill was created in the topsoil of the test section in different phases as follows. The flume was tilted at a gradient of five degrees and a discharge of $Q = 0.001$ m^3/s was applied for one minute duration. At the end of the one minute duration run, the flume was placed back to a horizontal position and a laser scanning device was employed to determine the longitudinal profile of the rill. Eighteen cross-sections spaced 0.1 m apart were measured. The entire

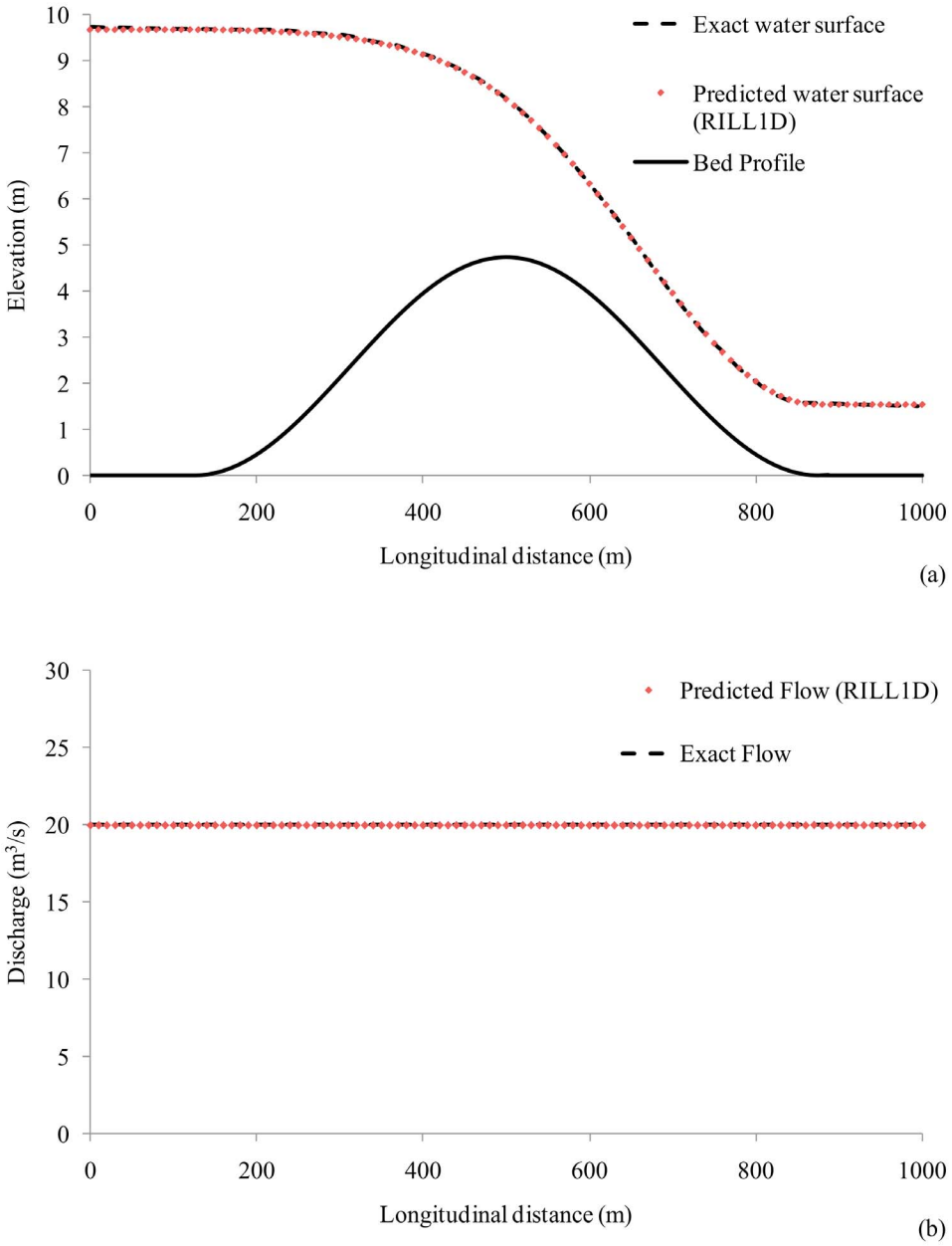

Figure 7. (a) Water surface profile of smooth flow in a rectangular, horizontal channel over a hump. Solid line shows the results from the RILL1D simulations and the dashed line provides the exact solution. (b) Flow continuity was preserved along the channel length.

process was repeated seven times (i.e., seven runs of one minute duration were performed under the same discharge). After seven minutes, a well defined rill was formed and the average flow velocity did not change significantly over time. At that time the topsoil surface was fixed by spraying polyester resin diluted in acetone. The flume bed was left intact for three to five hours to allow resin infiltration. By conducting dye tracing tests prior and after the application it was ensured that the resin did not affect the roughness characteristics of the rill bed. The flume was reset to its original slope used to create the rill (i.e., five degrees), and the same discharge of 0.001 m^3/s was applied. Flow depth measurements were collected along the longitude of the rill via the use of an elevation gage. A miniature Acoustic Doppler Velocimeter (ADV) (known also as micro ADV) was utilized to measure time averaged velocities near the bed and surface of the water column. The measurements were predominately obtained near the central axis of the rill. In some cases the micro ADV sensor was not fully submerged due to low flow depth, and hence, no measurements could be carried out. More details about the accuracy of velocity and limitations of the ADV technique are provided in *Giménez et al.* [2004]. According to *Giménez et al.* [2004] the rill bed morphology was characterized by a sequence of steps and pools. All steps had gradients similar to the average gradient of the rill and each step was between 150

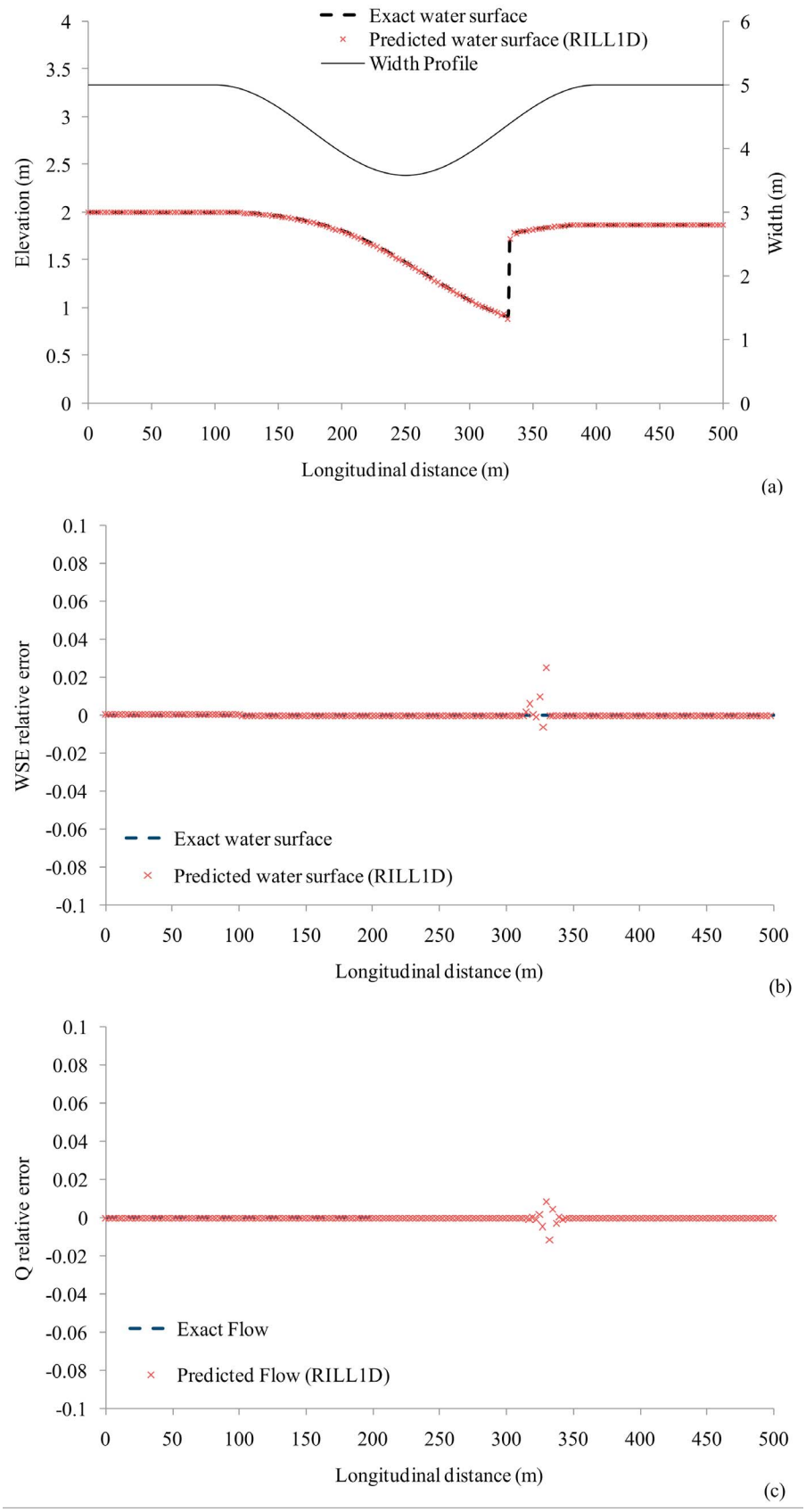

Figure 8. (a) Water surface profile of transcritical flow in a rectangular, horizontal, converging-diverging channel. Solid line shows the results from the RILL1D simulations and the dashed line provides the exact solution. (b, c) Relative errors in water surface elevation (*WSE*) and discharge (*Q*) along the channel length, respectively, between the exact and numerical solution.

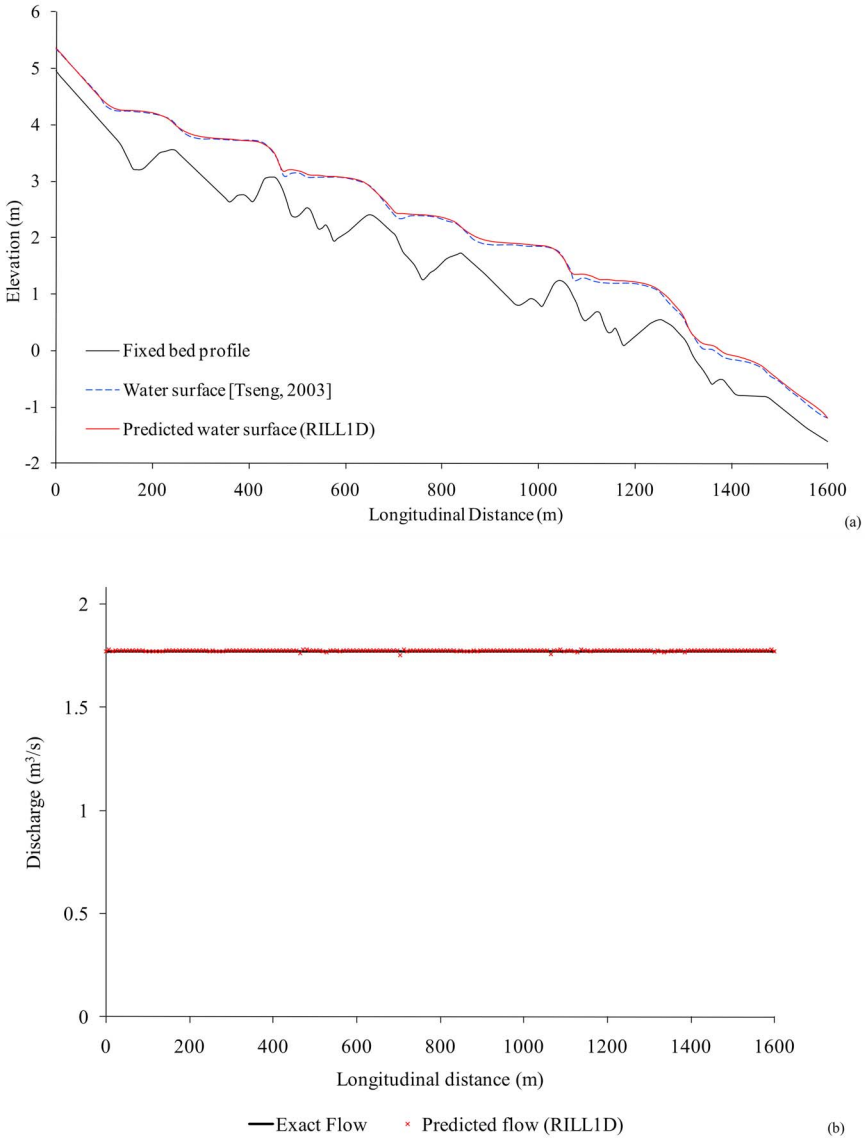

Figure 9. (a) Comparison of the water surface profiles of shallow water transcritical flow between the *Tseng* [2003] and RILL1D numerical simulations. (b) Comparison of the predicted and exact flow discharge for the *Tseng* [2003] case.

and 250 mm long. The average rill width was reported to be 70–80 mm, however, the width of the rill atop a pool brink was reduced to 25–30 mm.

[70] Herein, the bed morphology of the experimentally measured rill, shown in Figure 2 on page 108 of the *Giménez et al.* [2004] study, is digitized via software called *Datathief III v.1.5* and is incorporated into the numerical code as part of the input file. Because the rill geometry is quite abrupt (i.e., step-pool sequences and irregular cross-sections), we have incorporated all eighteen cross-sections as input in the model to reconstruct the rill longitudinal bed elevation profile. Due to brevity, we have not included this information in the main text, rather it can be found as supplementary material in Appendix A (Table A1). In addition, the experimentally measured width of the rill is carefully incorporated in the input file. Table 1 summarizes the hydraulic conditions used to simulate the *Giménez et al.* [2004] flume study. The Manning's n value is considered to range between 0.03 and 0.04 based on prior knowledge for flow in rills of similar geometry and flow conditions [*Foster and Meyer*, 1972].

[71] Figure 10 provides a comparison of the measured and predicted water surface profiles along the longitudinal direction of the rill (1.8 m). This simulation is performed using 400 cells and a discharge of $Q = 0.001$ m^3/s. It is shown that the improved surface gradient method, using the TVD-MacCormack scheme adequately simulates the variation of the water surface profile within the pools and atop the steps. The inclusion of the I_2 term (equation (5)) in the hydrodynamic component of the numerical code allows this code to account for the changes in the cross-sectional geometry along the longitudinal direction of the rill. This conservative form of the Saint-Venant equations overall guarantees jump intensities and celerities of surface waves [*Lax and Wendroff*, 1960]. The maximum error in the flow depth atop a step is around 8%, and the minimum is less

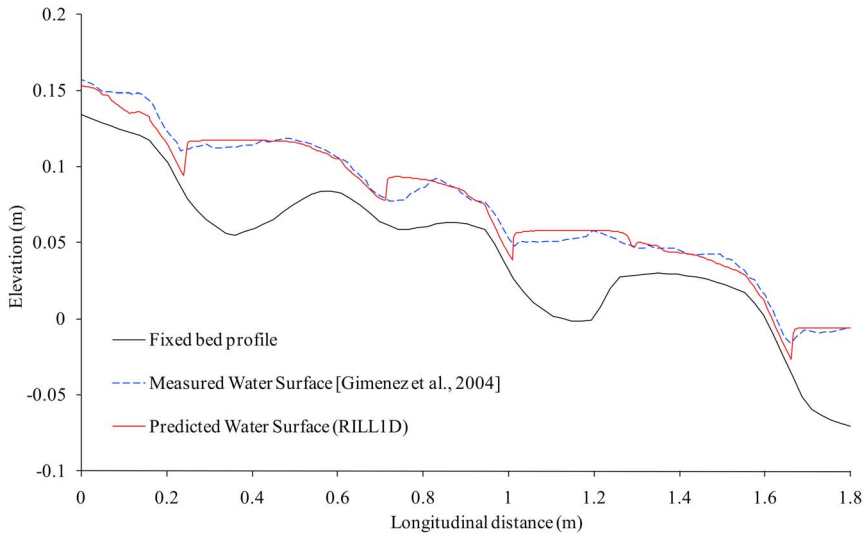

Figure 10. Profiles for data set 1 (400 cells).

than 1%. In the pools this error increases to a maximum value of 18% due to the three dimensional nature of flow. The minimum error in the pool is less than 2%. Despite this inherent limitation for flow in pools, RILL1D represents fairly accurate the flow patterns along the rill reach.

[72] The distribution of the predicted depth averaged velocity within the rill is presented in Figure 11. For comparison purposes, the measured surface and bed velocities are averaged per location along the rill. This is done because in pools, flow re-circulates and the bed velocities are predominately negative [e.g., *Giménez et al.*, 2004; *Römkens and Prasad*, 2005]. Averaging of the surface and bed velocity in shallow flows atop the steps is not necessary considering the bed and surface velocity vectors are of the same magnitude and direction. These averaged velocities are compared here against the predicted depth average velocities. RILL1D performs well above the step crests and at the downstream end (i.e., escape flow) of pools with an average error less than 10%. RILL1D underperforms as the approach flow enters the pool headwall and impinges within the pool volume. Two re-circulation eddies typically form within the pool leading to flow dissipation [*Giménez et al.*, 2004]. One forms near the surface with an anticlockwise circulation pattern, while the other one is a backroller which impinges against the pool headwall with negative velocity magnitudes [*Giménez et al.*, 2004]. As expected within the

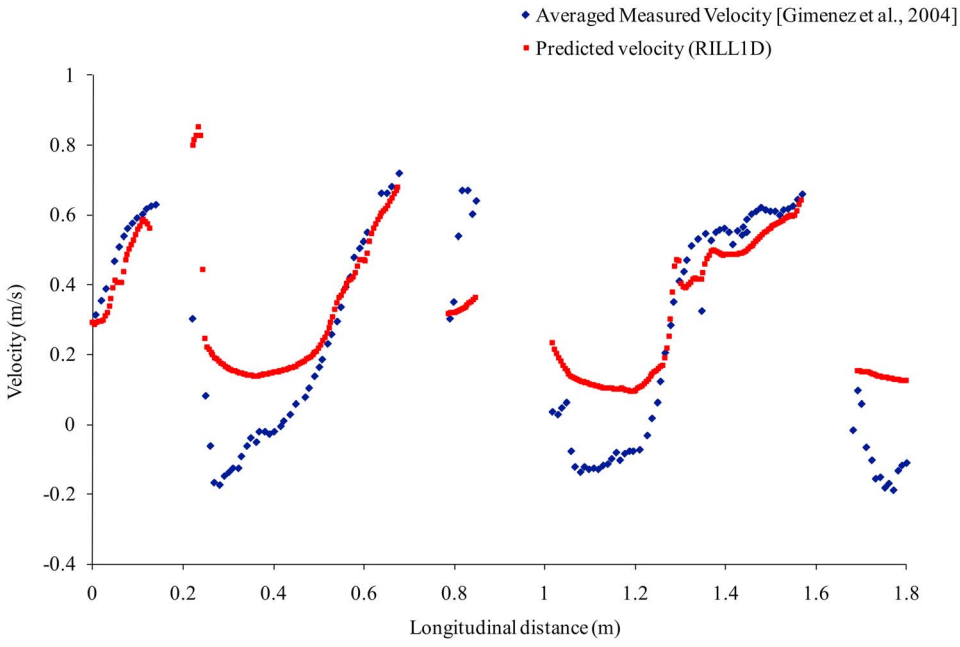

Figure 11. Streamwise distribution of velocities for data set 1 (400 cells).

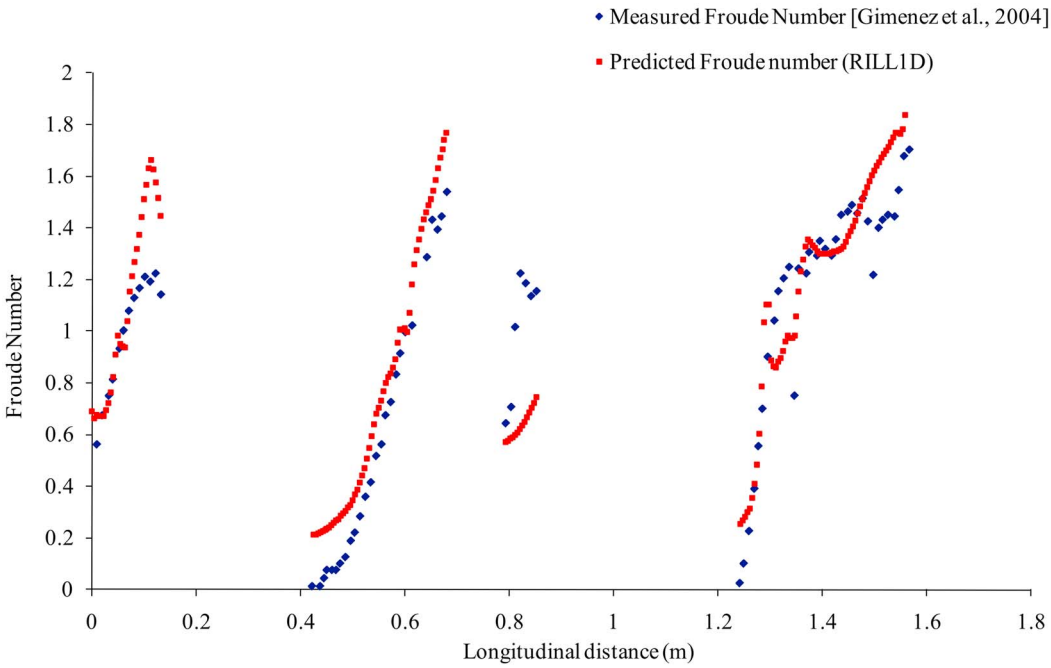

Figure 12. Froude numbers for data set 1 (400 cells).

pools, errors in the velocity magnitude of the predicted values ranges between 10–40%, primarily due to the presence of negative velocity magnitudes triggered by the backroller. Similar results have been reported by *Foster and Meyer* [1972], *Sadeghian and Mitchell* [1990], and *Bennett* [1999]. Figure 12 provides the Froude number spatial distribution and demonstrates that flow is transcritical at the brink of the pools.

[73] Figure 13 demonstrates that RILL1D satisfies the continuity equation for flow along the longitudinal direction of the rill. A small departure of the predicted discharge is observed only at the point where hydraulic jumps occur, i.e., three locations along the longitudinal direction of the rill. The average error in the predicted discharge for these three locations was approximately 13%.

[74] When the performance of the code for the *Giménez et al.* [2004] study is compared against the *Tseng* [2003]

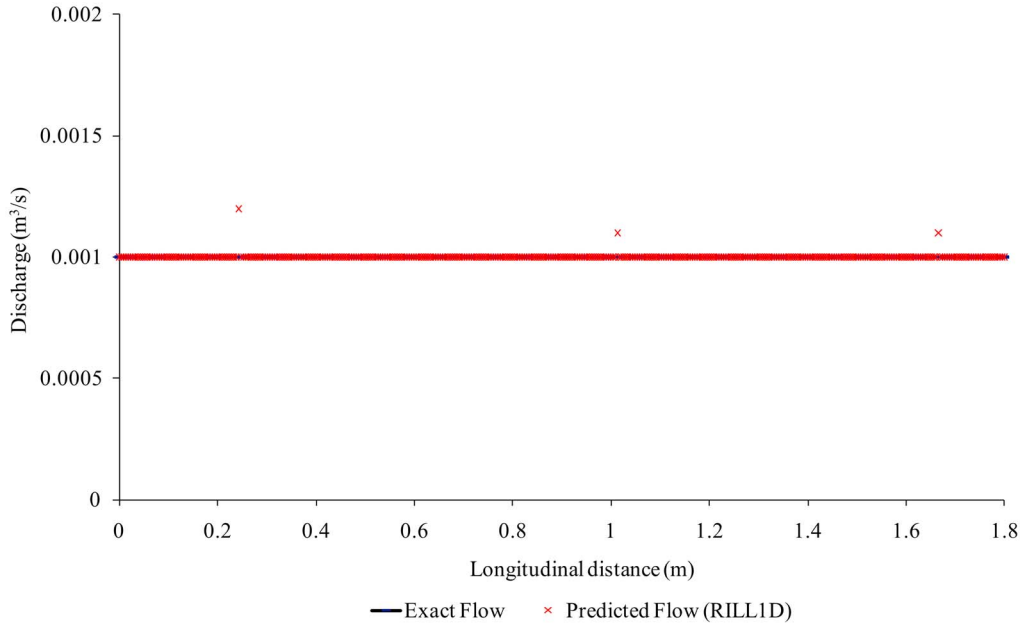

Figure 13. Discharge plot for data set 1 (400 cells).

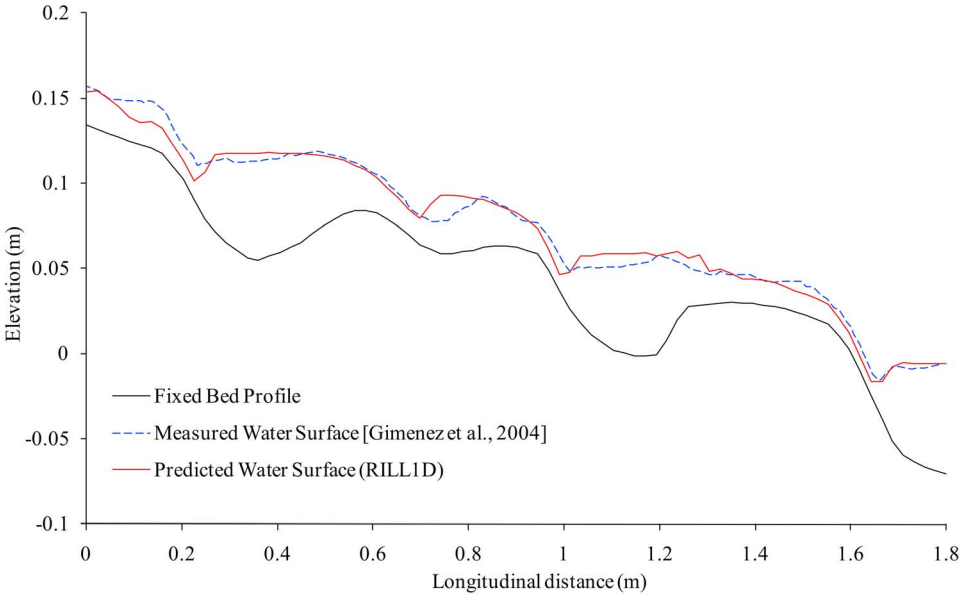

Figure 14. Profiles for data set 1 (80 cells).

case described earlier (or the benchmark test 4a), RILL1D clearly underperforms for the *Giménez et al.* [2004] test only at the entrance locations near the pools. We hypothesize that this difference is attributed to the shallow flow conditions (average flow of 1.0–2.0 cm) being present in the *Giménez et al.* [2004] experiment, in which the effects of the micro-roughness on flow are quite pronounced [*Tayfur et al.*, 1993]. The shallow flow conditions combined with an abrupt geometry are presumed to affect the model predictions near the pool entrances. Further, it is possible that despite the accuracy considered in the *Giménez et al.* [2004] rill geometry for the eighteen cross-sections, there is some departure from the experimental rill geometry for the segments found in-between the eighteen cross-sections. *Giménez et al.* [2004] do not provide specific information for these segments.

3.1.6. Cell Size Sensitivity Analysis for Fixed Bed Rill Simulations

[75] In order to examine the sensitivity of the model with respect to cell size, the *Giménez et al.* [2004] experimental case is simulated using 80 cells. In this case, Figure 14 shows that the model reproduced a similar water surface profile with that produced by using 400 cells. However, in Figure 15, one can notice that the model does not satisfy the flow continuity at the brink of the pools and the deviation of the discharge at those locations ranges between 10–40%.

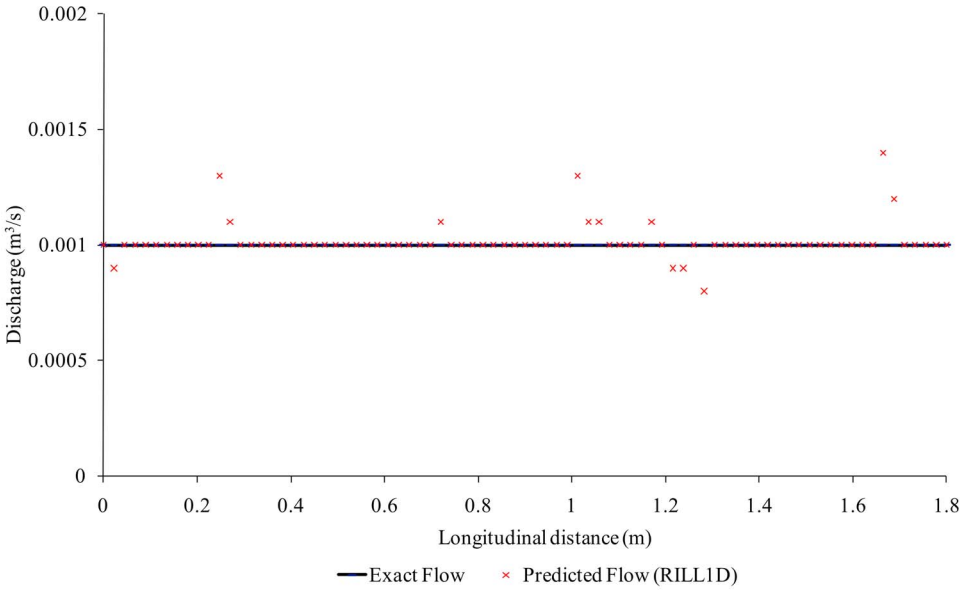

Figure 15. Discharge plot for data set 1 (80 cells).

Figure 16. The Mancilla rills in the Palouse. Posts indicate sampling locations (see sampling bottles placed at the measurement locations) [after *Mancilla*, 2004].

The comparison between the cases of 80 and 400 cells show that satisfaction of flow continuity is dependent upon cell size. Although the Courant number for both cases is less than 1, the solution using 80 cells is not oscillation free. Oscillations in the 80 cell run appear because both wave amplitude and wavelength are either delayed or accelerated in the numerical solution when compared to the exact solution [*Tseng*, 2003].

3.2. Numerical Tests to Examine the Sediment Component of RILL1D

[76] In order to test the sediment component of RILL1D, data sets were obtained from plot scale field experiments conducted in the Palouse region of Eastern Washington State [*Mancilla*, 2004]. The goals of these tests were to compare the predicted and experimentally determined water surface and bed profiles for different rill sections at the end of each experimental run as well as the sediment transport rates exiting the rills.

[77] Field experiments were conducted by *Mancilla* [2004] at the USDA Palouse Conservation Field Station in Pullman, WA. The main soil type characterizing this area is the semi cohesive Palouse silty-loam loess. The soil composition consists of 20.1% clay (primarily illite), 70.1% silt, and 9.8% fine sand. The average organic content of the Palouse soil is close to 2.6–3% [*Papanicolaou and Hilldale*, 2002]. *Van Klaveren and McCool* [1987] found a critical erosional strength, τ_c, close to 2.5 Pa when the Palouse ground was frozen and *Gilley et al.* [1993] and *Papanicolaou et al.* [2007] reported a τ_c of 4.5 Pa for the summer months. These two values yield an average τ_c of 3.5 Pa, which agrees well with the *Alberts et al.* [1995] formula (see equation (22)). According to *Gilley et al.* [1993], the erodibility factor, K_r, in equation (26) is equal to 0.00925 s/m.

[78] The reported experiments were conducted on bare soil at the beginning of the winter season 2003–2004, prior to the occurrence of the freeze-thaw (FT) cycle. The average longitudinal gradient of the farm, where the experimental runs were conducted, was equal to 23%. In order to develop the rills in the field, 2 cm deep incisions were made (Figure 16). These incisions were straight and predominately extended along the downslope direction. By following this incision approach, *Mancilla* [2004] generated five different incipient rills with almost identical characteristics. For each of these rills, *Mancilla* [2004] performed experiments for a wide range of flow rates, with the flow discharge, Q, being varied between 0.333×10^{-4} to 2.33×10^{-4} m^3/s. The different flow rates were replicated at least 6 times for each rill. The duration of the runs was approximately one hour. For each flow rate the rill was segmented into 1.5 to 3 m sections along the downslope (see polls in Figure 16 indicating the different cross-sections). Records of flow velocity, cross-sectional top width and average depth were collected for each section on an average every 15 min (Figure 16). The flow velocity was measured by florescent trace dye while the width and depth of the rill were captured with a measuring tape. Additionally, flow samples were taken at the rill outlet to determine the concentration of transported sediment. The porosity of the soil, θ, was reported to be quite small, equal to 0.005 [*Mancilla*, 2004]. This indicates that the soil was overall well compacted.

[79] This study focuses on two rills, namely, rill #3 and rill #4. For reference purposes, the same names are adopted here with those used by *Mancilla* [2004]. Rills #3 and #4 are simulated for two different discharges, though the geometry of the rills is different for the two flow rate runs per rill number. Table 2 summarizes the measured longitudinal distance, bed slope, width, Manning's roughness, depth at the rill centerline, discharge, median particle diameter, d_{50}, per cross-section. According to *Mancilla* [2004], rill #3 is 6 m long for both discharges (i.e., $Q = 0.000214$ m^3/s and $Q = 0.000217$ m^3/s), while rill #4 is 9 m long for one flow rate (i.e., $Q = 0.00012$ m^3/s) and 15 m long for the second flow rate (i.e., $Q = 0.000227$ m^3/s).

3.2.1. Cell Size and Critical Erosion Strength Sensitivity Analysis for Erodible Bed Rill Simulations

[80] The cell size sensitivity analysis was examined using 100, 200, 400, and 500 cells. For each cell, the critical erosional strength, τ_c, was varied within a physically meaningful range (i.e., a lower limit of 2.5 Pa for frozen soil and upper limit of 4.5 Pa for summer months), based on in-situ measurements in the Palouse region. In our sensitivity analysis, τ_c was varied between 2.0–5.0 Pa. This range of τ_c was used to determine the minimum required cell number in order to match the measured sediment transport rates reported by *Mancilla* [2004], at the end of the experimental runs, with the model's predicted sediment rates (accepted error less than 6%). Overall, 16 runs for each rill number were performed, but for brevity only the results of the cell size sensitivity analysis for rill #3 are presented herein (see Figure 17 and Table 3). For rill #3, the combination of a minimum cell number of 200 along with a τ_c of 4.55 Pa was required to satisfy flow continuity (Figure 17) and match the predicted transport rates with the *Mancilla* [2004] reported results (error 1.5% as seen in Table 3). The negative sign in

Table 2. Summary of *Mancilla* [2004] Rill Experiments

Rill Number	Cross-Section	Longitudinal Distance (m)	Slope (m/m)	Width (m)	Manning's Roughness	Depth (m)	Discharge (m^3/s)	Median Diameter (mm)
3	1	0	0.176	0.075	0.136	0.015	0.000214	0.0289
3	2	1.5	0.176	0.075	0.136	0.015	0.000214	0.0289
3	3	3	0.191	0.075	0.104	0.024	0.000214	0.0289
3	4	4.5	0.182	0.070	0.164	0.019	0.000214	0.0289
3	5	6	0.167	0.062	0.120	0.027	0.000214	0.0289
3	1	0	0.176	0.070	0.136	0.022	0.000217	0.0289
3	2	1.5	0.176	0.070	0.136	0.022	0.000217	0.028
3	3	3	0.191	0.090	0.166	0.020	0.000217	0.028
3	4	4.5	0.182	0.073	0.163	0.024	0.000217	0.028
3	5	6	0.167	0.060	0.123	0.024	0.000217	0.028
4	1	0	0.213	0.041	0.034	0.010	0.00012	0.0289
4	2	1.5	0.213	0.041	0.034	0.010	0.00012	0.0289
4	3	3	0.249	0.048	0.019	0.006	0.00012	0.0289
4	4	6	0.249	0.042	0.064	0.015	0.00012	0.0289
4	5	9	0.209	0.040	0.041	0.012	0.00012	0.0289
4	1	0	0.213	0.050	0.107	0.023	0.000227	0.0289
4	2	1.5	0.213	0.050	0.107	0.023	0.000227	0.0289
4	3	3	0.249	0.053	0.118	0.020	0.000227	0.0289
4	4	6	0.249	0.055	0.099	0.017	0.000227	0.0289
4	5	9	0.209	0.042	0.124	0.028	0.000227	0.0289
4	6	12	0.202	0.075	0.151	0.027	0.000227	0.0289
4	7	15	0.184	0.054	0.083	0.017	0.000227	0.0289

the error column of Table 3 implies that the predicted sediment transport rate was lesser in magnitude than the measured value. Similar sensitivity analyses were performed for all other rills to determine the minimum required number of cells.

[81] Table 4 provides comparison between measured and predicted sediment transport rates using *Yalin*'s [1977] transport capacity formula. It was constructed using different values of τ_c (between 2.0–5.0 Pa), for the minimum required number of cells determined for each rill case. For rill #4 (Q = 0.000227 m^3/s), the results of the sensitivity analysis show that the minimum required number of cells for satisfying flow continuity was equal to 500 for a τ_c = 5.0 Pa. The required number of cells in rill #4 was larger than rill #3 due to the longer rill length (i.e., rill #4 is 15 m whereas rill #3 is 6 m) (Table 4). By having 500 cells in the rill #4 run, the ratio of rill length to number of cells remained roughly the same with the corresponding ratio for rill #3. For rill #3 with slightly higher flow rate (Q = 0.00217 m^3/s), the optimum cell number was found to be 200 for a τ_c = 5.0 Pa (Table 4). In this case, a τ_c of 5.0 Pa resulted in only 2% error between predicted and measured sediment transport rates (Table 4).

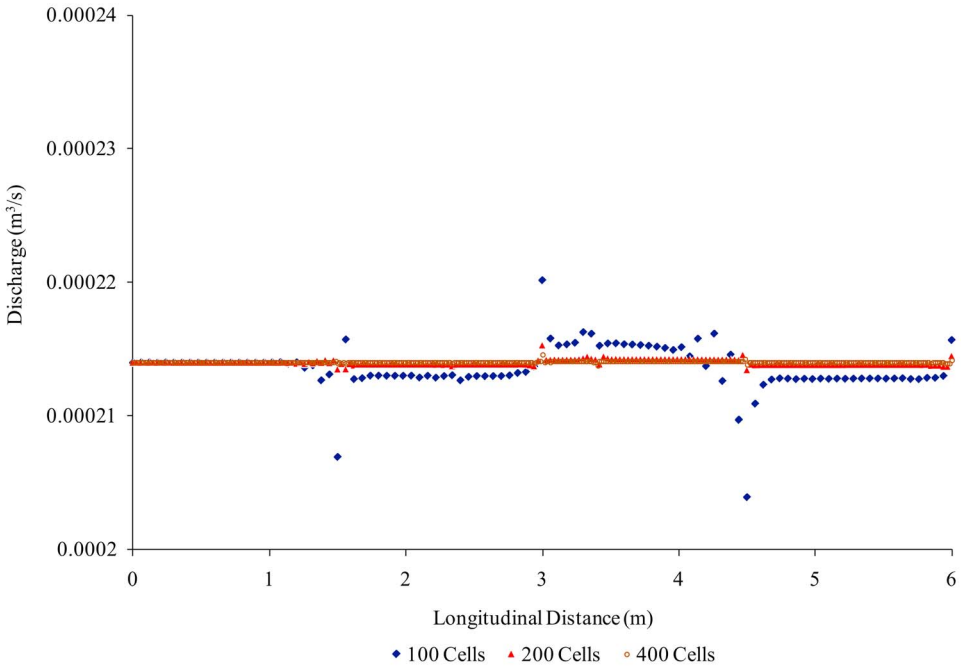

Figure 17. Discharge plot for rill #3 (Q = 0.000214 m^3/s).

Table 3. Cell Size Sensitivity Analysis for Rill #3[a]

Number of Cells	Predicted Sediment Transport Rate (10^{-7} m^3/s)	*Mancilla* [2004] Transport Rate (10^{-7} m^3/s)	Percent Error
100	1.806	1.96	−8.0
200	1.930	1.96	−1.5
400	1.926	1.96	−1.7

[a] Q = 0.000214 m^3/s, τ_c = 4.55 Pa.

[82] Last, for rill #4 (Q = 0.00012 m^3/s), the required number of cells was 200 and the τ_c value used in the simulations to match measured and predicted sediment transport rates was between 2.00 and 2.25 Pa (Table 4), which was the lower limit for τ_c values found in the Palouse. Although this value was within the range of reported values for Palouse soils, there was a difference between the required τ_c values for this particular simulation and all other runs. This can be explained as follows: (1) The flow rate for this run was almost half of all other flow rates, and it was possible that there were errors involved in accurately measuring the sediment transport rate for such shallow depths [*Mancilla*, 2004], and (2) the movement of sediment for such low flow, almost at near inception, was stochastic [*Nearing*, 1991]. It is possible the *Yalin* [1977] equation may have limited the code's ability to predict sediment movement for near inception conditions and thus we must lower the τ_c value to match predicted and measured sediment transport rates. Therefore, more research is needed to address the effects of turbulence on sediment movement for overland flows, as the majority of sediment formulas used are deterministic (see section 4).

3.2.2. Bed Morphodynamics

[83] Figures 18 and 19 provide a comparison of the predicted versus measured water surface and bed profiles at the end of the experimental runs for rill #3 (τ_c = 4.55 Pa, Q = 0.000214 m^3/s) and rill #4 (τ_c = 5.0 Pa, Q = 0.000227 m^3/s), respectively. Due to the small flow rates for the *Mancilla* [2004] tests, which were about 1/5 of the low rate reported in the *Giménez et al.* [2004] study, no step-pool formations were observed at the experimental site other than some localized bed scour holes. Because the relative differences between initial and final rill bed elevations are small, these are multiplied by a factor of 10 in order to make the bed elevation changes discernable to the reader (Figures 18 and 19). The same applies for the water surface elevations (predicted and measured) and the final measured bed elevations at the different rill cross-sections. Overall, RILL1D adequately replicates the final water surface and bed elevations for rill #3 using the *Yalin*'s [1977] transport capacity formula (see Figure 18). The average errors in the predicted water surface and bed elevations are approximately 12% and 6%, respectively.

[84] Along the same lines, results for rill #4 can be seen in Figure 19. Although, the water surface is simulated satisfactorily (average error less than 4%), the predicted bed topography using the *Yalin*'s [1977] transport capacity formula illustrates that RILL1D is unable to capture all of the localized bed erosion scour. Erosion evolves within the first 5.0 m of the section and no erosion/deposition occurs in the remaining reach (see Figure 19). Using *Yalin*'s [1977] equation, the model provided a maximum scour depth of ~1.3 cm, while the largest measured scour depth along the whole reach was ~1.9 cm.

4. Discussion and Conclusions

[85] This study entails the development of a numerical model for predicting hydrodynamic and sediment transport rates in rills. Replication of the rill conditions in terms of flow and bed evolution changes necessitated the use of an enhanced TVD-MacCormack scheme to provide an oscillation free solution (equations (13a) and (13b)). As a result, the dissipation terms in equations (13a) and (13b) are modified based on the surface gradient method proposed by *Tseng* [2003]. For this purpose, a characteristic variable, $\alpha_{i+1/2}$ (see equation (17)), is incorporated in the TVD dissipation term, Φ, in order to eliminate or reduce the artificial numerical error introduced by applying the TVD corrections to equations (13a) and (13b). In addition, the source terms of the bed and friction slopes were discretized using forward and backward differences (see equations (19a) and (19b)). Based on the results from the benchmark tests, it is shown that the enhanced TVD-MacCormack scheme adequately simulates transcritical flows by preserving the mass conservation and reducing the artificial numerical error. The scheme also approximates satisfactorily depth and velocity for a fixed bed rill with steps and pools, except near the pool headwalls where a backroller forms with negative velocities [e.g., *Foster and Meyer*, 1972]. With the inclusion of the gradient of σ with x, as shown in equation (5), the model is capable of accounting variable rill widths in space. A limitation is attached to this new feature; the width of different rill segments is considered to be time invariant during the simulation period.

Table 4. Results From Simulation of Rill Erosion Using *Yalin*'s [1977] Transport Capacity Formula for the Minimum Required Cell Number

Critical Erosional Strength (Pa)	Predicted Sediment Transport Rate (10^{-7} m^3/s)	*Mancilla* [2004] Transport Rate (10^{-7} m^3/s)	Percent Error
	Rill 3, Q = 0.000214 m^3/s, 200 Cells		
2.00	7.31	1.96	273
3.00	4.68	1.96	139
4.00	3.18	1.96	62
4.55	1.93	1.96	−1.5
5.00	2.74	1.96	40
	Rill 3, Q = 0.000217 m^3/s, 200 Cells		
2.00	7.54	1.37	450
3.00	4.82	1.37	252
4.00	3.38	1.37	147
5.00	1.40	1.37	2
	Rill 4, Q = 0.00012 m^3/s, 200 Cells		
2.00	2.09	1.61	30
2.25	1.38	1.61	−15
3.00	0.02	1.61	−99
4.00	0.00	1.61	NA
	Rill 4, Q = 0.000227 m^3/s, 500 Cells		
2.00	11.80	3.78	212
3.00	7.72	3.78	104
4.00	5.54	3.78	47
5.00	3.86	3.78	2

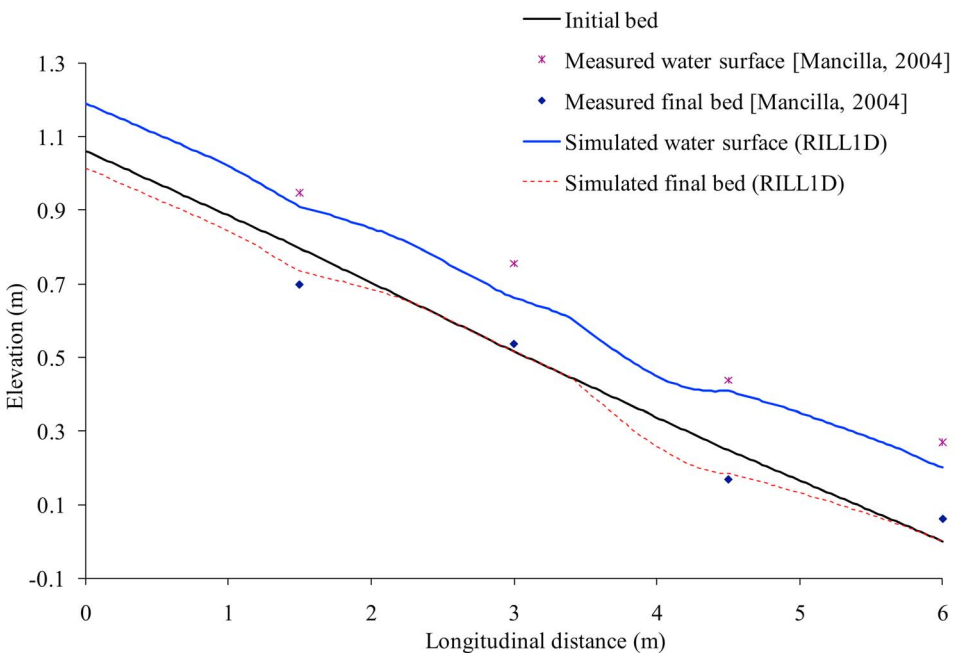

Figure 18. Rill #3 (Q = 0.000214 m^3/s, τ_c = 4.55 Pa). Comparison between measured and simulated water surface and bed elevation profiles using *Yalin*'s [1977] transport capacity formula. The distances of the water surface and final bed elevations from the initial bed have been scaled up by a factor of 10.

[86] The *Yalin* [1977] transport capacity equation (equation (23)), the *Foster et al.* [1995] equations for determining the detachment/deposition rates (equation (25)), and the *Alberts et al.* [1995] equations for calculating critical erosional strength in rills (equations (22a) and (22b)) are used to determine the net sediment volume and elevation changes within a cell. These equations allow for the modeling of finer, cohesive types of sediments comprised of clay, silt and sand in shallow flows [*Cochrane and Flanagan*, 1997]. With the field data provided by *Mancilla* [2004], the code is tested for its ability to reproduce measured values of sediment transport rates by using physically meaningful ranges of values for the critical erosional strength at the Palouse site (2.5–4.5 Pa). RILL1D performed reasonably

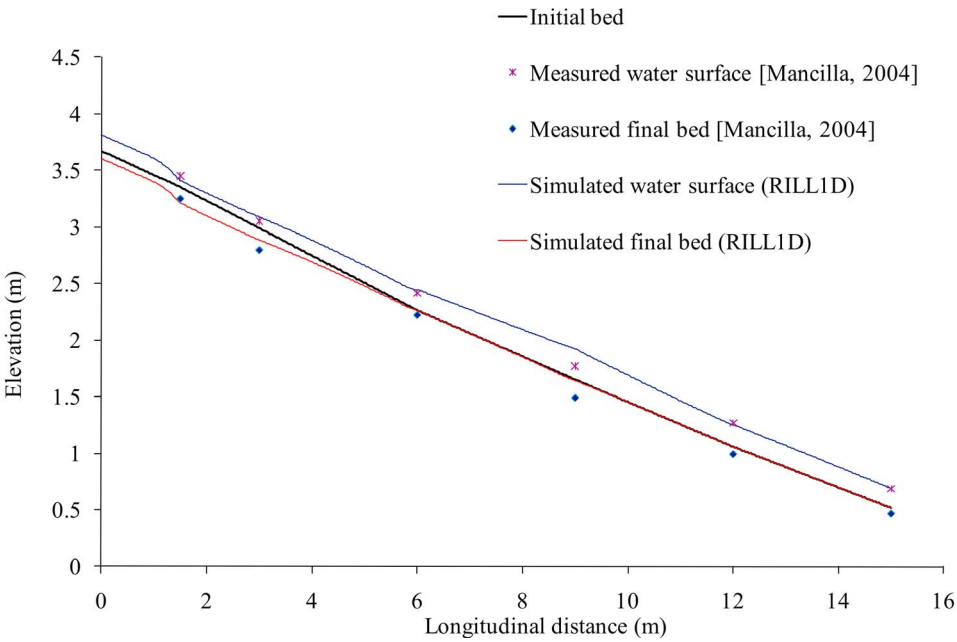

Figure 19. Rill #4 (Q = 0.000227 m^3/s, τ_c = 5.0 Pa). Comparison between measured and simulated water surface and bed elevation profiles using *Yalin*'s [1977] transport capacity formula. The distances of the water surface and final bed elevations from the initial bed have been scaled up by a factor of 10.

well in these simulations in terms of sediment prediction rates and fared adequately in terms of replicating rill bed morphology, at the end of the experimental runs and for different ranges of downslope, using *Yalin*'s [1977] sediment transport capacity formula. One caveat to our finding is that we have only tested a small number of sediment transport equations for estimating capacity and used two sets of simplified (to some degree controlled) field experiments where rills are artificially formed by incision than naturally. *Polyakov and Nearing* [2003] have shown that transport capacity differs, depending whether or not net detachment or net deposition occurs in the channel. Specifically, *Polyakov and Nearing* [2003] have found that sediment transport capacities differ by a factor of 2 when net depositional phase occurs as compared to net detachment, which should be accounted in the transport capacity formulas. Future work should be conducted for the development of transport capacity formulas that incorporate the resting period of particles within rill pools or in general over soil surface depression points. Incorporation of a lag time in most transport capacity formulas would help us better replicate the hysteretic nature of sediment movement. This effect could be significant when sediment moves across pools and steps, as it shown in our example with rill formation.

[87] Careful consideration of the cell size is necessary before using the code to predict sediment transport. We recommend a cell size sensitivity analysis to be performed for both the fixed bed and erodible bed rill simulations. The results show how cell size can affect the predictions of the TVD-MacCormack scheme (e.g., Figures 11, 15, and 17). It is seen in Table 3 that with all other parameters held constant, cell size, if incorrectly chosen, can produce vastly different sediment transport results. This was due to the conservation of mass being violated with the use of 100 cells (Figure 17). Once a particular number of cells is reached that satisfies flow continuity, the use of an even smaller cell size is not advantageous. Similarly, *Tayfur et al.* [1993] have shown that when the soil surface microtopography (or known interchangeably as random roughness) is represented at a very fine scale, all the local irregularities render the solution procedure of the Saint-Venant equations to become unstable. Thus, *Tayfur et al.* [1993] suggested that the local micro-topography needs to be smoothed out for the gradually varying flow assumption of the Saint-Venant equations to be applicable. In most cases, it is beneficial to run only the hydrodynamics to observe the continuity and then make a judgment on the number of cells to use. A rule of thumb is that the cell size should be larger than the median aggregate clod size, assuming that there is direct correspondence between clod size and surface micro-roughness. Based on this rule, in our study a range of 1–3 cm cell size was considered.

[88] Limitations of the model are evident. We must improve the critical erosion strength component of the model to account for the potential effects of freeze-thaw (FT) on soil strength. The *Mancilla* [2004] field experiments are performed in the winter time prior to thawing so the latter is not a factor in our study. However, when thawing occurs, we know soil particles and aggregates have less cohesional strength (bonding) comparatively to the strength at freezing conditions or during the summer period when the soil regains its strength [*Van Klaveren and McCool*, 1987; *Bullock et al.*, 1988]. According to *Gatto* [2000] and *Ferrick and Gatto* [2005], FT effects on strength are especially pronounced in newly thawed soils, when water content (WC) is fairly excessive (more than 20%) [*Maroufpoor et al.*, 2009]. High WC reduces particle interlocking and friction (according to the same authors FT effects on strength are minimal when WC is low). Potential improvements to be considered in RILL1D are the incorporation of additional parameters such as WC in revised critical erosional formulas to account for the effects of FT under different soil water contents.

[89] RILL1D does not consider the role of crop (or vegetation) residue on rill erodibility. As a result, the performance of the model is tested for the bare soil experiments of *Mancilla* [2004]. Yet, the presence of crop residue has been shown to reduce the bed shear stress exerted by the flow on rill beds, by minimizing the surface area exposed to the flow [see detailed experiments by *Giménez and Govers*, 2008], and decrease soil erosion rates [*Brown et al.*, 1989]. Future studies would benefit from a morphodynamic model that has the capability of incorporating residue cover (e.g., see the correction factor for residue cover in equation (4) [*Brown et al.*, 1989]).

[90] Preliminary laboratory experiments [*Dermisis and Papanicolaou*, 2009] and other studies [e.g., *Huang et al.*, 1999] show that subsurface flows and upward seepage effects (especially in saturated soils) can be extremely significant on rill erosion and sediment transport prediction. Findings from *Huang et al.* [1999] challenge the performance of existing transport capacity approaches when seepage effects are pronounced. Under these conditions, *Huang et al.* [1999] found that predicted transport capacity values underestimate the amount of eroded material, even at lower flow conditions. The consideration of subsurface flows above restrictive layers and upward seepage effects on the footslopes of hills, where saturated conditions are pronounced, is a needed improvement in predicting rill and any other type of concentrated flow erosion. While such limitation may not have a significant impact on long-term predictions (hundred year scale) of surface runoff and sediment erosion, the effects may be more pronounced for single storm predictions, which are events typically used to assess the performance of Best Management Practices (BMPs) [*Kennedy and Schillinger*, 2006; *Abaci and Papanicolaou*, 2009].

[91] The model does not account for the role of turbulence on sediment movement. The reason being is that we do not know as much about turbulence in overland flows as we do in river flows [e.g., *Nearing*, 1991]. Specifically, we do not know how turbulent stresses, intensities and kinetic energies vary in space and time in shallow overland flows, or how variations of those flow features may potentially signify entrainment events. Recent work by *Nikora et al.* [2007] on spectral velocity analysis for shallow unidirectional flows has shown that for high Froude numbers, flow resembles the structure of two-dimensional turbulence with an inverse energy cascade of that stated in Kolmogorov's theory. In this case, production of turbulence occurs near the surface instead of near the bed [*Papanicolaou and Hilldale*, 2002]. Therefore, more research is needed for adequately accounting for the role of turbulence on sediment movement in rill flows. Future research should also explore with the design of plot scale experiments, the turbulent flow characteristics under different slopes, soil micro-roughness,

Table A1. Input Data to Describe the Rill Longitudinal Bed Elevation Profile

Cross-Section	Bed Elevation (m)
1	0.1343
2	0.1227
3	0.1025
4	0.0604
5	0.0595
6	0.0749
7	0.0825
8	0.0641
9	0.0609
10	0.0629
11	0.0265
12	0.002
13	0.0077
14	0.029
15	0.0294
16	0.0222
17	0.0027
18	−0.0598

roughness induced by crop (or vegetation) residue, and rill macro-roughness (e.g., step-pool sequences).

[92] Finally, a key question that arises from this work is how we can incorporate such small-scale processes, which require detailed acquisition of data, and advanced modeling into a watershed model. It is certainly impractical, nearly impossible, to account for all rill features and associated processes at a watershed scale, where most of the geospatial models are designed to operate. Different strategies ought to be developed using predictions of the average rill morphological characteristics and their effect on longitudinal rill hydraulics, which can be easily incorporated into a process-based watershed model.

Appendix A

[93] To reconstruct the rill longitudinal bed elevation profile found in the *Giménez et al.* [2004] study all eighteen cross-sections were added as input in RILL1D. Table A1 presents the bed elevation data used in the RILL1D model.

Notation

A wetted cross-sectional area of the rill.
A_{bed} rill bed area.
b cell width.
B channel width.
c local wave celerity.
$clay$ clay content.
C_n Courant number.
d_{50} median particle diameter.
D_A active layer thickness.
D_f rate of rill detachment or deposition.
D_i interrill erosion.
DP_{pr} deposition depth of sediment with size class p and density r.
f Darcy-Weisbach coefficient.
$\boldsymbol{F}$ matrix for Saint-Venant equations.
F_{pr} percentage of the available particles with size class p and density r.
g acceleration of gravity.
G sediment load.
H flow depth.
i denotes space.
I_1 hydrostatic pressure force term.
I_2 term used to account for the changes in the cross-sectional geometry.
j denotes time.
k counter.
K_r rill erodibility parameter.
M number of different sediment class densities.
n Manning's resistance coefficient.
N number of different sediment class sizes.
N_1 counter of the different sediment class sizes that deposit.
N_2 counter of the different sediment class sizes that erode.
p sediment class size.
Q discharge.
q unit discharge.
R hydraulic radius.
$\boldsymbol{R}$ matrix for TVD dissipation term.
r sediment class density.
r_o characteristic ratio for the limiter parameter.
$\boldsymbol{S}$ matrix for Saint-Venant equations.
S_0 bed gradient.
SC_{pr} scour depth of sediment with size class p and density r.
S_f friction gradient.
SG particle specific gravity.
t time.
T_c sediment transport capacity.
u depth-averaged cross-sectional velocity.
$\boldsymbol{U}$ matrix for Saint-Venant equations.
V_f effective fall velocity.
vfs very fine sand.
WSE water surface elevation.
x denotes space.
z bed elevation.
α characteristic variable incorporated in the TVD dissipation term.
$\boldsymbol{\alpha}$ matrix for improved surface gradient method.
β momentum coefficient.
β_o dimensionless parameter in *Yalin*'s [1977] equation reflecting soil properties.
δ dimensionless parameter in *Yalin*'s [1977] equation reflecting soil properties.
ΔEL change in bed elevation.
Δt time step.
Δx cell space.
ε small positive number.
η water depth.
θ porosity.
λ parameter for the TVD dissipation term in the discharge calculation.
ρ water density.
ρ_s density of sediment particles.
σ channel width for a water depth η.
τ^* dimensionless bed shear stress acting on the rill bed.
τ_c dimensional critical shear stress.
τ_c^* dimensionless critical shear stress.
τ_o bed shear stress exerted by the fluid on the sediment particles.
ϕ flux limiter parameter.
$\boldsymbol{\Phi}$ matrix for TVD dissipation term.

χ raindrop-induced turbulent coefficient.
ψ entropy correction.
$(\sim)$ predictor step.
$(\approx)$ corrector step.
$\forall_{ACT}$ volume of available material in the active layer.
$\forall_{DP_{pr}}$ deposited volume of sediment with size class p and density r.
$\forall_{DR_{pr}}$ rill detachment volume of sediment with size class p and density r.
$\forall_{EC_{pr}}$ volume of excess capacity of sediment with size class p and density r.
$\forall_{IN_{pr}}$ volume inflow of sediment particles with size class p and density r.
$\forall_{\mathrm{sb}pr}$ volume of sediment carrying capacity with size class p and density r.
$\forall_{SC_{pr}}$ scour volume of sediment with size class p and density r.
$\forall_{OUT_{pr}}$ volume of sediment with size class p and density r that exits the cell.

References

Abaci, O., and A. N. Papanicolaou (2009), Long-term effects of management practices on water-driven soil erosion in an intense agricultural sub-watershed: Monitoring and modeling, *Hydrol. Processes*, *23*, 2818–2837, doi:10.1002/hyp.7380.

Alberts, E. E., M. A. Nearing, M. A. Weltz, L. M. Risse, F. B. Pierson, X. C. Zhang, J. M. Laflen, and J. R. Simanton (1995), Soil component, in *USDA-Water Erosion Prediction Project: Hillslope Profile and Watershed Model Documentation, Rep. 10*, edited by D. C. Flanagan and M. A. Nearing, chap. 7, pp. 1–47, Natl. Soil Erosion Res. Lab., Agric. Res. Serv., U.S. Dep. of Agric., West Lafayette, Indiana.

Alonso, C. V., W. H. Neibling, and G. R. Foster (1981), Estimating sediment transport capacity in watershed modeling, *Trans. ASAE*, *24*(5), 1211–1220.

Bennett, S. J. (1999), Effect of slope on the growth and migration of headcuts in rills, *Geomorphology*, *30*(3), 273–290, doi:10.1016/S0169-555X(99)00035-5.

Bennett, S. J., and C. V. Alonso (2006), Turbulent flow and bed pressure within headcut scour holes due to plane reattached jets, *J. Hydraul. Res.*, *44*(4), 510–521.

Black, K. S., T. J. Tolhurst, D. M. Paterson, and S. E. Hagerthey (2002), Working with natural cohesive sediments, *J. Hydraul. Eng.*, *128*(1), 2–8, doi:10.1061/(ASCE)0733-9429(2002)128:1(2).

Bradford, S. F., and B. F. Sanders (2002), Finite-volume model for shallow-water flooding of arbitrary topography, *J. Hydraul. Eng.*, *128*(3), doi:10.1061/(ASCE)0733-9429(2002)128:3(289).

Brown, L. C., G. R. Foster, and D. B. Beasley (1989), Rill erosion as affected by incorporated crop residue and seasonal consolidation, *Trans. ASAE*, *32*(6), 1967–1978.

Brufau, P., P. Garcia-Navarro, P. Ghilardi, L. Natale, and F. Savi (2000), 1D mathematical modeling of debris flow, *J. Hydraul. Res.*, *38*(6), 435–446.

Bullock, M. S., W. D. Kemper, and S. D. Nelson (1988), Soil cohesion as affected by freezing, water content, time and tillage, *Soil Sci. Soc. Am. J.*, *52*, 770–776.

Cao, Z., G. Pender, and P. Carling (2006), Shallow water hydrodynamic models for hyperconcentrated sediment-laden floods over erodible bed, *Adv. Water Resour.*, *29*, 546–557, doi:10.1016/j.advwatres.2005.06.011.

Catella, M., E. Paris, and L. Solari (2008), Conservative scheme for numerical modeling of flow in natural geometry, *J. Hydraul. Eng.*, *134*(6), 736–748, doi:10.1061/(ASCE)0733-9429(2008)134:6(736).

Chaudhry, M. H. (1993), *Open Channel Flow*, 2nd ed., 523 pp., Prentice Hall, Englewood Cliffs, N. J.

Cochrane, T. A., and D. C. Flanagan (1997), Detachment in a simulated rill, *Trans. ASAE*, *40*(1), 111–119.

Cunge, J. A., F. M. Holly Jr., and A. Verwey (1980), *Practical Aspects of Computational River Hydraulics*, 420 pp., Pitman, London.

Dermisis, D., and A. N. Papanicolaou (2009), Effects of rainfall-runoff on soil surface roughness and erosion processes, paper presented at the World Environmental and Water Resources Congress, Am. Soc. of Civ. Eng., Kansas City, Mo., 17–21 May.

De Santisteban, L. M., J. Casalí, J. J. López, J. V. Giráldez, J. Poesen, and J. Nachtergaele (2005), Exploring the role of topography in small channel erosion, *Earth Surf. Processes Landforms*, *30*(5), 591–599, doi:10.1002/esp.1160.

Elliot, W. J., and J. M. Laflen (1993), A process-based rill erosion model, *Trans. ASAE*, *36*, 65–72.

Ferrick, M. G., and L. W. Gatto (2005), Quantifying the effect of a freeze-thaw cycle on soil erosion: Laboratory experiments, *Earth Surf. Processes Landforms*, *30*(10), 1305–1326, doi:10.1002/esp.1209.

Finkner, S. C., M. A. Nearing, G. R. Foster, and J. E. Gilley (1989), A simplified equation for modeling sediment transport capacity, *Trans. ASAE*, *32*(5), 1545–1550.

Flanagan, D. C., and M. A. Nearing (2000), Sediment particle sorting on hillslope profiles in the WEPP model, *Trans. ASAE*, *43*(3), 573–583.

Foster, G. R., and L. D. Meyer (1972), Transport of soil particles by shallow flow, *Trans. ASAE*, *15*(1), 99–102.

Foster, G. R., D. C. Flanagan, M. A. Nearing, L. J. Lane, L. M. Risse, and S. C. Finkner (1995), Hillslope erosion component, in *USDA-Water Erosion Prediction Project: Hillslope Profile and Watershed Model Documentation, Rep. 10*, edited by D. C. Flanagan and M. A. Nearing, chap. 11, pp. 1–47, Natl. Soil Erosion Res. Lab., Agric. Res. Serv., U.S. Dep. of Agric., West Lafayette, Indiana.

Garcia-Navarro, P., F. Alcrudo, and J. M. Saviron (1992), 1-D open channel flow simulation using TVD-MacCormack scheme, *J. Hydraul. Eng.*, *118*(10), 1359–1372, doi:10.1061/(ASCE)0733-9429(1992)118:10(1359).

Gatto, L. W. (2000), Soil freeze–thaw-induced changes to a simulated rill: Potential impacts on soil erosion, *Geomorphology*, *32*(1–2), 147–160, doi:10.1016/S0169-555X(99)00092-6.

Gharangik, A. M., and M. H. Chaudhry (1991), Numerical simulation of hydraulic jump, *J. Hydraul. Eng.*, *117*, 1195–1211, doi:10.1061/(ASCE)0733-9429(1991)117:9(1195).

Gilley, J. E., W. J. Elliot, J. M. Laflen, and J. R. Simanton (1993), Critical shear stress and critical flow rates for initiation of rilling, *J. Hydrol.*, *142*(1–4), 251–271, doi:10.1016/0022-1694(93)90013-Y.

Giménez, R., and G. Govers (2008), Effects of freshly incorporated straw residue on rill erosion and hydraulics, *Catena*, *72*(2), 214–223, doi:10.1016/j.catena.2007.05.004.

Giménez, R., O. Planchon, N. Silvera, and G. Govers (2004), Longitudinal velocity patterns and bed morphology interaction in a rill, *Earth Surf. Processes Landforms*, *29*(1), 105–114, doi:10.1002/esp.1021.

Giménez, R., J. Léonard, Y. Duval, G. Richard, and G. Govers (2007), Effect of bed topography on soil aggregates transport by rill flow, *Earth Surf. Processes Landforms*, *32*(4), 602–611, doi:10.1002/esp.1418.

Govers, G., R. Giménez, and K. Van Oost (2007), Rill erosion: Exploring the relationship between experiments, modelling and field observations, *Earth Sci. Rev.*, *84*(3–4), 87–102, doi:10.1016/j.earscirev.2007.06.001.

Hancock, G. R., D. Crawter, S. G. Fityus, J. Chandler, and T. Wells (2007), The measurement and modelling of rill erosion at angle of repose slopes in mine spoil, *Earth Surf. Processes Landforms*, *33*(7), 1006–1020, doi:10.1002/esp.1585.

Harten, A., and J. Hyman (1983), Self-adjusting grid methods for one-dimensional hyperbolic conservation laws, *J. Comput. Phys.*, *50*(2), 235–269, doi:10.1016/0021-9991(83)90066-9.

Huang, C., L. K. Wells, and L. D. Norton (1999), Sediment transport capacity and erosion processes: Model concepts and reality, *Earth Surf. Processes Landforms*, *24*(6), 503–516, doi:10.1002/(SICI)1096-9837(199906)24:6<503::AID-ESP972>3.0.CO;2-T.

Kennedy, A. C., and W. F. Schillinger (2006), Soil quality and water intake in conventional-till vs. no-till paired farms in Washington's Palouse region, *Soil Sci. Soc. Am. J.*, *70*, 940–949, doi:10.2136/sssaj2005.0160.

Lax, P. D., and B. Wendroff (1960), Systems of conservation laws, *Commun. Pure Appl. Math.*, *13*, 217–237, doi:10.1002/cpa.3160130205.

Lei, T. W., M. A. Nearing, K. Haghighi, and V. F. Bralts (1998), Rill erosion and morphological evolution: A simulation model, *Water Resour. Res.*, *34*(11), 3157–3168, doi:10.1029/98WR02162.

LeVeque, R. J. (2002), *Finite Volume Methods for Hyperbolic Problems*, Cambridge Univ. Press, Cambridge, U. K.

Lindley, M. R., B. J. Barfield, and B. N. Wilson (1995), Surface impoundment element model description, in *USDA-Water Erosion Prediction Project: Hillslope Profile and Watershed Model Documentation, Rep. 10*, edited by D. C. Flanagan and M. A. Nearing, chap. 14, pp. 1–28, Natl. Soil Erosion Res. Lab., Agric. Res. Serv., U.S. Dep. of Agric., West Lafayette, Indiana.

Liu, Q. Q., L. Chen, J. C. Li, and V. P. Singh (2007), A non-equilibrium sediment transport model for rill erosion, *Hydrol. Processes*, *21*(8), 1074–1084, doi:10.1002/hyp.6288.

MacCormack, R. W. (1969), The effect of viscosity in hypervelocity impact cratering, in *Frontiers of Computational Fluid Dynamics*, edited by D. A. Caughey and M. M. Hafez, pp. 27–44, Am. Inst. of Aeronaut. and Astronaut., Cincinnati, Ohio.

Mancilla, G. A. (2004), Critical shear stress and rill sediment transport capacity of Palouse soil, Ph.D. dissertation, 146 pp., Coll. of Eng. and Arch., Wash. State Univ., Pullman.

Mancilla, G. A. (2005), Rill density prediction and flow velocity distributions on agricultural areas in the Pacific Northwest, *Soil Tillage Res.*, *84*(1), 54–66, doi:10.1016/j.still.2004.10.002.

Maroufpoor, I., S. Emamgholizadeh, H. Torabi, and M. Behzadinasab (2009), Impact of soil texture on the calibration of TDR for water content measurement, *J. Appl. Sci.*, *9*(16), 2933–2940, doi:10.3923/jas.2009.2933.2940.

Morgan, R. P. C., J. N. Quinton, R. E. Smith, G. Govers, J. W. A. Poesen, K. Auerswald, G. Chisci, D. Torri, and M. E. Styczen (1998), The European Soil Erosion Model (EUROSEM): A dynamic approach for predicting sediment transport from fields and small catchments, *Earth Surf. Processes Landforms*, *23*(6), 527–544, doi:10.1002/(SICI)1096-9837(199806)23:6<527::AID-ESP868>3.0.CO;2-5.

Nearing, M. A. (1991), A probabilistic model of soil detachment by shallow turbulent flow, *Trans. ASAE*, *34*(1), 81–85.

Nearing, M. A., L. D. Norton, D. A. Bulgakov, G. A. Larionov, L. T. West, and K. M. Dontsova (1997), Hydraulics and erosion in eroding rills, *Water Resour. Res.*, *33*(4), 865–876, doi:10.1029/97WR00013.

Nikora, V., R. Nokes, W. Veale, M. Davidson, and G. Jirka (2007), Large-scale turbulent structure of uniform shallow free-surface flows, *Environ. Fluid Mech.*, *7*(2), 159–172, doi:10.1007/s10652-007-9021-z.

Nord, G., and M. Esteves (2007), Evaluation of sediment transport formulae and detachment parameters in eroding rills using PSEM_2D and the Water Erosion Prediction Project (WEPP) database, *Water Resour. Res.*, *43*, W08420, doi:10.1029/2006WR005444.

Øygarden, L. (2003), Rill and gully development during an extreme winter runoff event in Norway, *Catena*, *50*(2–4), 217–242, doi:10.1016/S0341-8162(02)00138-8.

Papanicolaou, A. N., and R. Hilldale (2002), Turbulence characteristics in gradual channel transition, *J. Eng. Mech.*, *128*(9), 948–960, doi:10.1061/(ASCE)0733-9399(2002)128:9(948).

Papanicolaou, A. N., A. Bdour, and E. Wicklein (2004), One-dimensional hydrodynamic/sediment transport model applicable to steep mountain streams, *J. Hydraul. Res.*, *42*(4), 357–375.

Papanicolaou, A. N., M. Elhakeem, and R. Hilldale (2007), Secondary current effects on cohesive riverbank erosion, *Water Resour. Res.*, *43*, W12418, doi:10.1029/2006WR005763.

Partheniades, E. (2009), *Cohesive Sediments in Open Channels, Properties, Transport and Applications*, 384 pp., Butterworth-Heinemann, Burlington, Vt.

Polyakov, V. O., and M. A. Nearing (2003), Modelling sediment transport from bare rilled hillslopes by areally averaged transport equations, *Catena*, *51*, 33–43, doi:10.1016/S0341-8162(02)00090-5.

Römkens, M. J., and S. Prasad (2005), Hydrologically driven mechanisms of headcut development, *Int. J. Sediment Res.*, *20*(3), 176–184.

Sadeghian, M. R., and J. K. Mitchell (1990), Hydraulics of micro-braided channels: Resistance to flow on tilled soils, *Trans. ASAE*, *33*(2), 458–468.

Sanders, B. F., D. A. Jaffe, and A. K. Chu (2003), Discretization of integral equations describing flow in nonprismatic channels with uneven beds, *J. Hydraul. Eng.*, *129*(3), doi:10.1061/(ASCE)0733-9429(2003)129:3(235).

Tatard, L., O. Planchon, J. Wainwright, G. Nord, D. Favis-Mortlock, N. Silvera, O. Ribolzi, M. Esteves, and C. Huang (2008), Measurement and modelling of high-resolution flow-velocity data under simulated rainfall on a low-slope sandy soil, *J. Hydrol.*, *348*(1–2), 1–12, doi:10.1016/j.jhydrol.2007.07.016.

Tayfur, G. (2002), Applicability of sediment transport capacity models for nonsteady state erosion from steep slopes, *J. Hydrol. Eng.*, *7*(3), 252–259, doi:10.1061/(ASCE)1084-0699(2002)7:3(252).

Tayfur, G. (2007), Modelling sediment transport from bare rilled hillslopes by areally averaged transport equations, *Catena*, *70*, 25–38, doi:10.1016/j.catena.2006.07.002.

Tayfur, G., and M. L. Kavvas (1994), Spatially averaged conservation equations for interacting rill-interrill area overland flows, *J. Hydraul. Eng.*, *120*(12), 1426–1448, doi:10.1061/(ASCE)0733-9429(1994)120:12(1426).

Tayfur, G., and M. L. Kavvas (1998), Areally averaged overland flow equations at hillslope scale, *Hydrol. Sci. J.*, *43*(3), 361–378, doi:10.1080/02626669809492132.

Tayfur, G., M. L. Kavvas, R. S. Govindaraju, and D. E. Storm (1993), Applicability of St. Venant equations for two dimensional overland flow over rough infiltrating surfaces, *J. Hydraul. Eng.*, *119*, 51–63, doi:10.1061/(ASCE)0733-9429(1993)119:1(51).

Thoman, R. W., and S. L. Niezgoda (2008), Determining erodibility, critical shear stress, and allowable discharge estimates for cohesive channels: Case study in the Powder River Basin of Wyoming, *J. Hydraul. Eng.*, *134*(12), 1677–1687, doi:10.1061/(ASCE)0733-9429(2008)134:12(1677).

Thorne, C. R., and L. W. Zevenbergen (1985), Estimating mean velocity in mountain rivers, *J. Hydraul. Eng.*, *111*(4), 612–624, doi:10.1061/(ASCE)0733-9429(1985)111:4(612).

Toro, E. F. (2001), *Shock-Capturing Methods for Free-Surface Shallow Flows*, John Wiley, Chichester, U. K.

Torri, D., J. Poesen, L. Borselli, and A. Knapen (2006), Channel width-flow discharge relationships for rills and gullies, *Geomorphology*, *76*(3–4), 273–279, doi:10.1016/j.geomorph.2005.11.010.

Tseng, M. (2003), The improved surface gradient method for flows simulation in variable bed topography channel using TVD-MacCormack scheme, *Int. J. Numer. Methods Fluids*, *43*(1), 71–91, doi:10.1002/fld.605.

Van Klaveren, R. W., and D. K. McCool (1987), Hydraulic erosion resistance of thawing soil, *Pap. 87-2602*, Am. Soc. of Agric. Eng., St. Joseph, Mich.

Vázquez-Cendón, M. E. (1999), Improved treatment of source terms in upwind schemes for the shallow water equations in channels with irregular geometry, *J. Comput. Phys.*, *148*, 497–526, doi:10.1006/jcph.1998.6127.

Yalin, M. S. (1977), *Mechanics of Sediment Transport*, 2nd ed., 298 pp., Pergamon, London.

Yee, H. C. (1989), A class of high-resolution explicit and implicit shock-capturing methods, *NASA Tech. Memo., NASA-TM 101088*.

D. C. Dermisis and A. N. Papanicolaou, IIHR-Hydroscience and Engineering, Department of Civil and Environmental Engineering, University of Iowa, Iowa City, IA 52242, USA. (apapanic@engineering.uiowa.edu)

G. A. Mancilla, Departamento de Silvicultura, Facultad de Ciencias, Universidad de Chile, 10 Forestales, Casilla 9206, Santiago, Chile.

J. T. Sanford, WEST Consultants, Seattle, WA 98005, USA.